

Effects of chemically homogeneous evolution of the first stars on the 21-cm signal and reionization

Boyuan Liu^{1,2}, Daniel Kessler^{3,4}, Thomas Gessey-Jones^{3,5}, Jiten Dhandha^{1,5},
Anastasia Fialkov^{1,5}, Yves Sibony⁶, Georges Meynet⁶, Volker Bromm^{7,8}, and Rennan Barkana⁹

¹*Institute of Astronomy, University of Cambridge, Madingley Road, Cambridge, CB3 0HA, UK*

²*Institut für Theoretische Astrophysik, Zentrum für Astronomie, Universität Heidelberg, Albert Ueberle Straße 2, D-69120 Heidelberg, Germany*

³*Astrophysics Group, Cavendish Laboratory, J. J. Thomson Avenue, Cambridge, CB3 0HE, UK*

⁴*School of Mathematical and Physical Sciences, University of Sheffield, Hounsfield Road, Sheffield, S3 7RH, UK*

⁵*Kavli Institute for Cosmology, Madingley Road, Cambridge, CB3 0HA, UK*

⁶*Observatoire de Genève, Chemin Pegasi 51, 1290 Versoix, Switzerland*

⁷*Department of Astronomy, University of Texas, Austin, TX 78712, USA*

⁸*Weinberg Institute for Theoretical Physics, University of Texas, Austin, TX 78712, USA*

⁹*Department of Astrophysics, School of Physics and Astronomy, Tel Aviv University, Tel Aviv 69978, Israel*

Accepted XXX. Received YYY; in original form ZZZ

ABSTRACT

The first generation of stars, known as Population III (Pop III), played a crucial role in the early Universe through their unique formation environment and metal-free composition. These stars can undergo chemically homogeneous evolution (CHE) due to fast rotation, becoming more compact and hotter/bluer than their (commonly assumed) non-rotating counterparts. In this study, we investigate the impact of Pop III CHE on the 21-cm signal and cosmic reionization under various assumptions on Pop III star formation, such as their formation efficiency, initial mass function, and transition to metal-enriched star formation. We combine stellar spectra computed by detailed atmosphere models with semi-numerical simulations of Cosmic Dawn and the Epoch of Reionization ($z \sim 6 - 30$). The key effect of CHE arises from the boosted ionizing power of Pop III stars, which reduces the Pop III stellar mass density required to reproduce the observed Thomson scattering optical depth by a factor of ~ 2 . Meanwhile, the maximum 21-cm global absorption signal is shallower by up to ~ 15 mK (11%), partly due to the reduced Lyman-band emission from CHE, and the large-scale ($k \sim 0.2$ cMpc⁻¹) power drops by a factor of a few at $z \gtrsim 25$. In general, the effects of CHE are comparable to those of Pop III star formation parameters, showing an interesting interplay with distinct features in different epochs. These results highlight the importance of metal-free/poor stellar evolution in understanding the early Universe and suggest that future studies should consider joint constraints on the physics of star/galaxy formation and stellar evolution.

Key words: stars: Population III – stars: chemically peculiar – dark ages, reionization, first stars – early Universe

1 INTRODUCTION

The first generation of stars, the so-called Population III (Pop III), are expected to be fundamentally different from their present-day Population I/II (Pop I/II) counterparts due to their unique primordial formation environment and metal-free nature (reviewed by, e.g., Bromm et al. 2009; Bromm 2013; Haemmerlé et al. 2020; Klessen & Glover 2023). As they form in primordial gas with inefficient cooling, Pop III stars tend to be more massive than Pop I/II stars. Their initial mass function (IMF) is typically broad and top-heavy, extending to $\sim 10^3 M_{\odot}$ and even higher masses ($\sim 10^4 - 10^6 M_{\odot}$) in extreme cases (e.g., Greif et al. 2011, 2012; Susa et al. 2014; Hirano et al. 2014, 2015, 2018; Stacy et al. 2016; Hirano & Bromm 2017; Susa 2019; Sugimura et al. 2020; Wollenberg et al. 2020; Chon et al. 2021; Sharda et al. 2020, 2021; Sharda & Krumholz 2022; Latif et al. 2022;

Riaz et al. 2022a; Prole et al. 2022a, 2023; Toyouchi et al. 2023). Besides, if magnetic braking is inefficient¹ (Stacy et al. 2011, 2013; Hirano & Bromm 2018; Kimura et al. 2023), Pop III stars will be born as fast rotators due to rapid accretion ($\sim 0.01 - 1 M_{\odot} \text{ yr}^{-1}$) of gas with high angular momentum from hot, thick star-forming disks in the protostar phase. The initial rotation velocities can reach a fraction of $\sim 0.5 - 1$ of the critical value (i.e., equatorial Keplerian velocity).

Under such peculiar conditions and due to the lack of metals,

¹ The roles played by magnetic fields in Pop III star formation including their impact on fragmentation of primordial star-forming disks and initial spins of Pop III stars are still in debate (McKee et al. 2020; Sharda et al. 2020, 2021; Sharda & Krumholz 2022; Hirano et al. 2021; Prole et al. 2022b; Saad et al. 2022; Stacy et al. 2022; Hirano & Machida 2022; Sadanari et al. 2023, 2024; Sharda & Menon 2024). In extreme cases, the rotation of Pop III (proto)stars can be slowed down by exponentially amplified magnetic fields (Hirano & Machida 2022).

* E-mail: boyuan.liu@uni-heidelberg.de

† E-mail: jvd29@cam.ac.uk

‡ E-mail: afialkov@ast.cam.ac.uk

stellar evolution and feedback of Pop III stars are also very different from those of Pop I/II stars (e.g., Schaerer 2002; Meynet et al. 2006; Ekström et al. 2008; Heger & Woosley 2010; Yoon et al. 2012; Tanikawa et al. 2020; Murphy et al. 2021; Aryan et al. 2023; Martinet et al. 2023; Nandal et al. 2023; Volpato et al. 2023; Costa et al. 2025), producing unique signatures in direct observations (e.g., strong HeII and Lyman- α emission and extremely blue UV spectra, Windhorst et al. 2018; Grisdale et al. 2021; Nakajima & Maiolino 2022; Vikaeus et al. 2022; Trussler et al. 2023; Katz et al. 2023; Larkin et al. 2023; Venditti et al. 2024; Zackrisson et al. 2011, 2012; Zackrisson et al. 2024; Lecroq et al. 2025)² and imprints in cosmic chemical and thermal evolution (see, e.g., Karlsson et al. 2013; Frebel & Norris 2015; Barkana 2016; Dayal & Ferrara 2018 for reviews), which allow us to constrain their properties through indirect probes.

For instance, the chemical imprints of metal enrichment from Pop III stars can be recorded in extremely metal-poor ($[\text{Fe}/\text{H}] \lesssim -3$) stars in the local Universe as bona-fide second-generation stars, which provide essential hints on the mass distribution, nucleosynthesis, and supernova (SN) properties of Pop III stars (e.g., Frebel & Norris 2015; Ji et al. 2015; Ishigaki et al. 2018; Koutsouridou et al. 2023; Vanni et al. 2023). In fact, nucleosynthesis features of strong mixing induced by fast rotation in massive stars are found in the chemical patterns of extremely metal-poor stars observed in the local Universe (e.g., Chiappini et al. 2006, 2011; Chiappini 2013; Maeder et al. 2015; Choplin et al. 2017, 2019; Liu et al. 2021b; Jeena et al. 2023), which supports the massive and fast-rotating nature of Pop III stars. The strong nitrogen and carbon enhancement in high- z galaxies observed by the James Webb Space Telescope (JWST, Bunker et al. 2023; D'Eugenio et al. 2023; Cameron et al. 2023; Senchyna et al. 2023; Ji et al. 2024; Schaerer et al. 2024; Sodini et al. 2024; Topping et al. 2024) can also be explained by the peculiar metal yields of fast-rotating Pop III stars (Nandal et al. 2024; Tsiatsiou et al. 2024). In particular, the very high carbon (C) enhancement in the most metal-poor ($[\text{Fe}/\text{H}] \lesssim -4$) stars (see, e.g., Yoon et al. 2016, 2018; Hansen et al. 2019; Dietz et al. 2021; Zepeda et al. 2023) can be explained by the carbon-rich (post main sequence) winds from fast-rotating massive Pop III stars (Liu et al. 2021b; Jeena et al. 2023). Moreover, the highest C enhancement seen in observations with absolute abundances³ $A(\text{C}) \gtrsim 7$ requires Pop III stars to reach a chemically homogeneous (CH) state that can significantly boost carbon production (Jeena et al. 2023).

Such chemically-homogeneous evolution (CHE) is the extreme limit of efficient mixing from rotational-induced instabilities (e.g., Yoon et al. 2006; Brott et al. 2011; Szécsi et al. 2015, 2022), which has interesting consequences on the properties, feedback, and observational signatures of massive stars (Eldridge & Stanway 2012; Szécsi et al. 2015, 2022; Kubátová et al. 2019; Sibony et al. 2022; Liu et al. 2025) and their remnants, such as Wolf-Rayet stars (Martins et al. 2009, 2013), pair-instability supernovae (Yoon et al. 2012; du Buisson et al. 2020; Umeda & Nagele 2024), gamma-ray bursts (Yoon & Langer 2005; Yoon et al. 2006, 2012), and binary com-

pact object mergers (de Mink & Mandel 2016; Mandel & de Mink 2016; Marchant et al. 2017, 2023; du Buisson et al. 2020; Riley et al. 2021; Qin et al. 2023; Vigna-Gómez et al. 2025). Beyond unique metal enrichment, Pop III stars with CHE will be more compact and hotter than in the (standard) non-rotating (NR) case and can potentially burn most of their hydrogen into helium during their main sequence (MS), so that their UV emission will also be different. It is shown in Sibony et al. (2022) that CHE significantly boosts the emission of ionizing photons from Pop III stars (and their escape from minihaloes), which accelerates cosmic reionization, producing a Thomson scattering optical depth up to 5σ higher than the observed value $\tau_0 = 0.0544 \pm 0.0073$ (Planck Collaboration 2020) in the most extreme case of high star formation efficiency (SFE)⁴. This shows that the fraction of Pop III stars and their SFE can be constrained by observations of τ_0 . However, Sibony et al. (2022) adopt an idealized analytical model for early star formation and reionization that only considers Pop III stars at $z > 15$ and extrapolate the high- z results to predict the full reionization history so that their results should be regarded as upper limits.

In addition to reionization, the UV radiation from Pop III stars, especially Lyman-band photons, also shapes the 21-cm signal from neutral hydrogen during Cosmic Dawn and the Epoch of Reionization (EoR), which is a promising probe of early structure/star formation at $z \sim 6-30$ (e.g., Fialkov et al. 2013; Fialkov & Barkana 2014; Mirocha & Furlanetto 2019; Schauer et al. 2019; Chatterjee et al. 2020; Qin et al. 2020; Gessey-Jones et al. 2022; Kamran et al. 2022; Magg et al. 2022a; Muñoz et al. 2022; Bevins et al. 2023; Hassan et al. 2023; Mondal & Barkana 2023; Ventura et al. 2023; Fialkov et al. 2023). In light of this, we extend the previous work by Sibony et al. (2022) to explore the effects of Pop III CHE on both reionization and the 21-cm signal with state-of-the-art semi-numerical simulations (see Gessey-Jones et al. 2023 and references therein), which self-consistently model the formation and feedback of Pop III and Population II (Pop II) stars and follow (spatially-resolved) evolution of the intergalactic medium (IGM) from $z = 50$ down to $z = 6$.

Beyond stellar UV radiation, X-rays, primarily from X-ray binaries (XRBs), also play important roles in the thermal and ionization evolution of IGM during Cosmic Dawn and EoR (e.g., Fragos et al. 2013b; Fialkov et al. 2014b; Pacucci et al. 2014; Madau & Fragos 2017; Eide et al. 2018; Kaur et al. 2022; Gessey-Jones et al. 2025), particularly at $z \lesssim 20$, via heating (and ionization) that can cause the transition of the global 21-cm signal from absorption to emission around $z \sim 10-15$ (Fialkov et al. 2014b), although theoretical predictions on the contribution of Pop III XRBs are uncertain especially when CHE is involved. It is shown in Sartorio et al. (2023) that the population-averaged X-ray emission efficiency of XRBs from NR Pop III stars can be significantly higher (up to a factor of 40) compared with that of Pop II XRBs (Fragos et al. 2013a,b) in optimistic cases (see also Ryu et al. 2016). However, if Pop III stars undergo CHE, they remain compact throughout their lifetimes, such that very close ($\lesssim 30 R_\odot$) binaries are required to trigger Roche lobe overflow (RLOF), which is the main mechanism of forming Pop III XRBs identified in Sartorio et al. (2023). It is still in debate whether such

² Although several promising candidates for Pop III systems have been detected (e.g., Welch et al. 2022; Schauer et al. 2022; Wang et al. 2024; Vanzella et al. 2023; Maiolino et al. 2024; Zackrisson et al. 2024; Fujimoto et al. 2025), direct observations of a representative sample of Pop III stars are still challenging in the near future (Gardner et al. 2006; Angel et al. 2008; Rhodes et al. 2020; Schauer et al. 2020; Katz et al. 2022; Nakajima & Maiolino 2022; Riaz et al. 2022b).

³ $A(\text{C}) \equiv \log(N_{\text{C}}/N_{\text{H}}) + 12$, where N_{C} and N_{H} are the number abundances of carbon and hydrogen, respectively. Throughout this paper, \log denotes the logarithm of base 10.

⁴ Strong emission of ionizing photons from Pop III stars can result in a double-reionization scenario (Cen 2003) with the first full ionization event happening at $z \gtrsim 10$ (Salvador-Solé et al. 2017), which can explain recent observations of Lyman- α ($\text{Ly}\alpha$) emitting galaxies (Salvador-Solé et al. 2022). Very massive ($\sim 100-10^3 M_\odot$) Pop III stars are required to produce this double-reionization feature if they evolve normally, while less massive ($\sim 10 M_\odot$) Pop III stars can be sufficient if they undergo CHE with boosted ionizing power (Sibony et al. 2022).

close binaries of Pop III stars exist as Pop III binary statistics are highly sensitive to the poorly understood properties of Pop III star clusters (Liu et al. 2021a)⁵. Besides, previous studies focusing on RLOF XRBs find that the donor star must avoid CHE in order to expand and transfer mass to the compact companion (Marchant et al. 2017). Here, we make the simplifying assumption that all Pop III stars undergo CHE and cannot produce RLOF XRBs. In reality, hybrid populations of CHE and non-CHE stars are likely more common, and the presence of Pop III XRBs from RLOF and other mechanisms⁶ is still possible. Since the focus of this paper is the impact of enhanced UV emission from CHE, we turn off the X-ray emission from Pop III XRBs for simplicity and adopt an observationally-motivated model for Pop II XRBs (see Sec. 3.3). We defer a comprehensive investigation of the UV emission and XRBs from CH Pop III stars in future work (for the results for NR Pop III stars, see Gessey-Jones et al. 2025).

The paper is organized as follows. In Section 2, we calculate the UV spectra from Pop III stars with CHE and discuss how they are different from those in the widely-used NR case. In Section 3, we introduce our framework of semi-numerical simulations, with emphasis on the updates in the modelling of ionization with respect to the version used in Gessey-Jones et al. (2023) and the parameter space explored. In Section 4, we present our predictions on the 21-cm signal (Sec. 4.3) and cosmic ionization history (Sec. 4.2). Finally, we summarize our findings and discuss their implications in Section 5.

2 UV RADIATION FROM THE FIRST STARS

In this paper, we focus on the UV radiation from the first stars, particularly Lyman-band and ionizing photons, that regulate the 21-cm signal and ionization history during Cosmic Dawn. In this section, we calculate the spectra and ionizing photon production rates of chemically-homogeneous Pop III stars, which are compared with those for NR Pop III stars from Gessey-Jones et al. (2022). The latter include stars (logarithmically-spaced) in the mass range of $M_{\star} \sim 0.5\text{--}500 M_{\odot}$ evolved by the code MESA (version 12115, Paxton et al. 2019) up to the end of MS⁷ (i.e., core hydrogen depletion) with no mass loss, whose spectra are derived using the same stellar code adopted here (see below).

For simplicity, we only consider (hydrogen-burning) MS that produces the majority of UV photons. We derive the MS stellar evolution histories for a grid of 12 (initial) stellar masses $M_{\star} = 9, 12, 15, 20, 30, 40, 60, 85, 120, 180, 250, 300 M_{\odot}$ using the polytrope CHE model detailed in Sibony et al. (2022), assuming no mass loss. This

⁵ In fact, it is found by recent radiative hydrodynamic simulations of primordial star formation (Sugimura et al. 2020, 2023; Park et al. 2023, 2024) that Pop III protostars tend to migrate outwards due to accretion of gas with high angular momentum, implying that close ($\lesssim 100$ AU) binaries of massive Pop III stars are likely rare. If this is true, the X-ray emission from Pop III RLOF XRBs will be negligible (Liu et al. 2021a).

⁶ Other than RLOF XRBs, CH Pop III stars are more likely to produce winded XRBs (that do not require very close binaries) via strong Wolf-Rayet winds (Qiu et al. 2019; Zuo et al. 2021) or the ‘Be-phenomenon’ in which a fast-rotating star ejects materials to a decretion disk that a compact companion can accrete from (Reig 2011; Rivinius et al. 2013; Liu et al. 2024a). However, such scenarios have not been systematically explored for CH stars.

⁷ In Gessey-Jones et al. (2022), the MESA runs of stars with $M_{\star} \sim 310\text{--}500 M_{\odot}$ do not reach the end of MS but stop when the star starts to photoevaporate. The subsequent Lyman-band emission is expected to be negligible and ignored (see their appendix a). In this work, we focus on stars below $300 M_{\odot}$ whose spectra throughout MS are available.

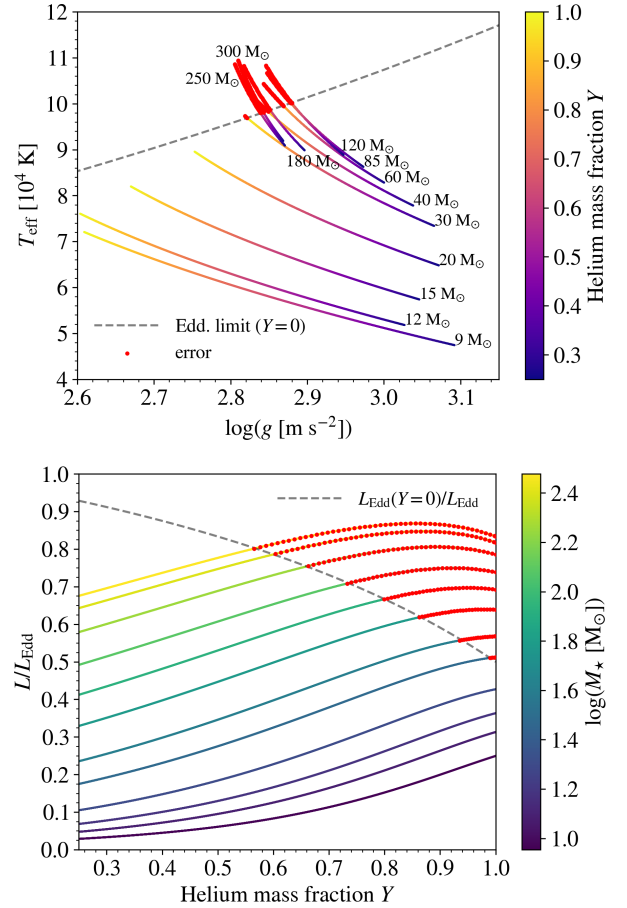


Figure 1. MS evolution of CH Pop III stars in terms of effective temperature T_{eff} versus logarithm of surface gravity g (upper) and Eddington ratio versus helium mass fraction Y (lower). In the upper panel, the evolution tracks are color coded by Y as an evolution stage indicator. The Eddington limit for atmospheres purely made of hydrogen ($Y = 0$) is shown with the dashed curve. In the lower panel, the evolution tracks are color coded by stellar mass M_{\star} . Now the dashed curve denotes the ratio between the Eddington limit for fully ionized pure hydrogen ($Y = 0$) and that for hydrogen-helium plasma with varying Y , i.e., $L_{\text{Edd}}(Y = 0)/L_{\text{Edd}}(Y) = \mu_{\text{e}}^{-1} = (1 - 0.75Y)/(1 - 0.5Y)$. In both panels, the cases where the stellar atmosphere code TLUSTY fails to converge to a statistic atmosphere are highlighted in red, which occur in late-stage evolution of massive stars ($M_{\star} \gtrsim 30 M_{\odot}$) when the Eddington limit for pure hydrogen is exceeded. An extrapolation scheme is developed to cover this regime based on the trend of spectra shape evolution in the rest of the parameter space with converged results (see Eq. A1 and the text below).

analytical approach well captures the compact, hot nature of CH stars that is responsible for their enhanced far and extreme UV radiation. The resulting evolution tracks in the HR diagram (fig. 1 in Sibony et al. 2022) are consistent with those from detailed stellar evolution simulations (e.g., Szécsi et al. 2015, see their fig. 5) for the majority of MS ($Y \lesssim 0.9$). In general, both luminosity and effective temperature increase with time under CHE, while stars without CHE tend to expand significantly and cool down. The mass range of Pop III stars is still in debate in theory, which is expected to vary with the conditions of star formation (e.g., Liu et al. 2024b). For simplicity, we adopt a fixed range $M_{\star} \in [9, 300] M_{\odot}$ that is broadly consistent with observational constraints on the (global average) IMF of Pop III stars (Hartwig et al. 2022, 2024).

As an improvement of the previous results in Sibony et al. (2022)

which adopted black-body spectra, we use the stellar atmosphere code TLUSTY⁸ (version 205, Hubeny 1988; Hubeny & Lanz 2017a,b,c; Hubeny et al. 2021) to calculate the spectra of each star at several time steps⁹ throughout MS given the corresponding effective temperature T_{eff} , surface gravity g and chemical abundances. Here we ignore the trace amount of metals synthesized during MS, so that the chemical composition of the atmosphere is completely determined by the (overall) helium mass fraction Y of a CH Pop III star. The top panel of Fig. 1 shows the evolution tracks of the 12 stars in the space of T_{eff} and $\log(g)$, colour-coded by Y , which serves as a good evolution stage indicator, since our CH stars burn all hydrogen into helium, reaching $Y = 1$ at the end of MS. Contrary to the case of NR Pop III stars (see fig. 2 in Gessey-Jones et al. 2022 and fig. 1 in Sibony et al. 2022) where T_{eff} generally decreases with time during MS, CH Pop III stars become hotter as Y increases for $M_{\star} \sim 9 - 300 M_{\odot}$. The reason is that CH stars remain compact (i.e., very little expansion)¹⁰ despite the luminosity enhancement from increasing Y .

At each point on the evolution track chosen for spectrum calculation, we adopt the TLUSTY settings and iterative procedure described in Gessey-Jones et al. (2022, see their Sec. 3.4) to search for a converged atmosphere model¹¹. Converged results are obtained for most cases in the relevant parameter space with $g \sim 10^{2.6-3.1} \text{ m s}^{-2}$ and $T_{\text{eff}} \lesssim 9.6 \times 10^4 \text{ K}$, while TLUSTY fails for the hottest atmospheres that occur in late-stage ($Y \gtrsim 0.6$) evolution of massive ($M_{\star} \gtrsim 30 M_{\odot}$) CH stars. After close scrutiny, we find that these atmospheres will be super Eddington if they are purely made of hydrogen, i.e., the radiation pressure from Thomson scattering for ionized hydrogen exceeds the gravity at the stellar surface. However, considering the high abundances of helium mixed into them during CHE, these atmospheres will approach but still remain below the Eddington limit¹², as shown in the lower panel of Fig. 1. It seems that TLUSTY always assumes the existence of a layer of pure hydrogen in the atmosphere, and the computation fails to converge to a static atmosphere when this hydrogen layer becomes super Eddington. In reality, the atmospheres of massive fast-rotating CH Pop III stars may indeed be unstable when they approach the Eddington limit by the end of MS ($Y \gtrsim 0.6$), such that they can enter the Wolf-Rayet phase with non-negligible mass loss (a few percent of the initial mass) enhanced by fast rotation and surface enrichment of heavy elements (e.g., C, N, O, and Fe) that boosts the opacity of the atmosphere (e.g., Jeena et al. 2023). This scenario is not considered in our analytical CHE model. Here, we assume that mass loss is negligible for CH Pop III stars throughout MS, i.e., until complete hydrogen depletion ($Y = 1$), so that our results should be regarded as optimistic estimates. Under this assumption, we develop a simple extrapolation scheme to compute the late-stage

⁸ We use TLUSTY because it has been successfully applied to massive (Pop III) stars (Schaerer 2002; Lanz & Hubeny 2003, 2007; Gessey-Jones et al. 2022). In particular, the spectra of NR Pop III stars from Gessey-Jones et al. (2022), which serve as the reference to compare our CHE results with, are computed using TLUSTY.

⁹ The time steps are chosen such that the variations in $\log(T_{\text{eff}})$ and $\log(g)$ are less than 0.01 dex at each step.

¹⁰ For $M_{\star} \sim 9 - 300 M_{\odot}$, the stellar radii of CH Pop III stars increase by $\Delta R_{\star} = 0.9 \pm 0.2 R_{\odot}$ during MS, almost independent of M_{\star} , while those of NR Pop III stars increase by $\Delta R_{\star} \sim 2 - 100 R_{\odot}$, reaching up to ~ 10 times of the zero-age MS value (see table 1 in Sibony et al. 2022).

¹¹ Convergence is achieved when the variations of all atmosphere properties are less than 1% for an iteration in TLUSTY.

¹² The Eddington luminosity L_{Edd} of fully ionized hydrogen-helium plasma is proportional to the number of electrons per baryon $\mu_e = (1 - 0.5Y)/(1 - 0.75Y)$ which increases with the helium mass fraction Y .

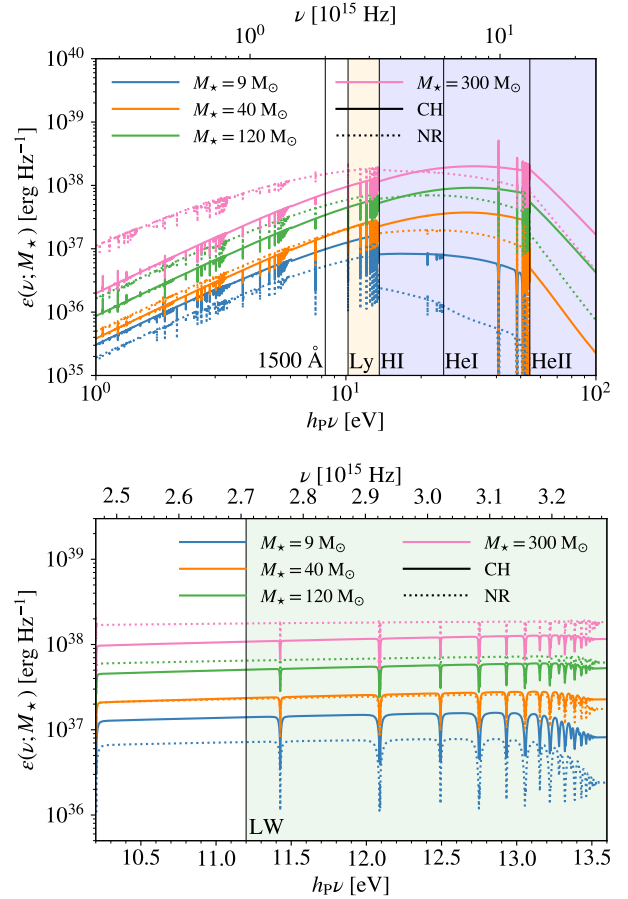


Figure 2. MS lifetime-integrated spectra of CH (solid) and NR (dotted) Pop III stars with masses of $M_{\star} = 9, 40, 120$ and $300 M_{\odot}$ (from bottom to top). The upper panel shows the spectra in the photon energy range of $h_p \nu \in [1, 100] \text{ eV}$, where the vertical lines label the characteristic energies for Lyman-band (Ly, $h_p \nu \sim 10.2 - 13.6 \text{ eV}$, orange shaded area), hydrogen (HI, $h_p \nu > 13.6 \text{ eV}$), helium first (HeI, $h_p \nu > 24.6 \text{ eV}$) and second (HeII, $h_p \nu > 54.4 \text{ eV}$) ionizing photons, and rest-frame UV at 1500 \AA corresponding to $h_p \nu \approx 8.3 \text{ eV}$. The spectrum at $h_p \nu > 13.6 \text{ eV}$ (blue shaded area) is integrated to calculate the production rate of (hydrogen) ionizing photons. The lower panel zooms into the Lyman band ($h_p \nu \sim 10.2 - 13.6 \text{ eV}$), where the energy/frequency range of H_2 -dissociating Lyman-Werner (LW) photons ($h_p \nu \sim 11.2 - 13.6 \text{ eV}$) are highlighted by the shaded area. The spectra of NR stars are derived by interpolation (over mass) of the spectra in Gessey-Jones et al. (2022). We use h_p to denote the Planck constant to avoid confusion with the Hubble constant parameter h in cosmology.

spectra of the 8 stars with $M_{\star} \geq 30 M_{\odot}$ for which TLUSTY results are unavailable, as discussed in Appendix A. It is shown in Kubátová et al. (2019, see their fig. 2) that for the maximum (effective) surface metallicity $Z \sim 10^{-4}$ achievable in Pop III CH stars (Jeena et al. 2023), the impact of Wolf-Rayet-like winds on the spectra of CH stars with $M_{\star} \sim 20 - 130 M_{\odot}$ at $h_p \nu \sim 8 - 54.4 \text{ eV}$ is always negligible for the majority of MS ($Y \lesssim 0.98$) under various wind prescriptions. Therefore, the ignorance of mass loss is not expected to change our conclusions.

Since we only consider massive ($M_{\star} \geq 9 M_{\odot}$) stars with short MS lifetimes $t_{\text{MS}} \lesssim 30 \text{ Myr}$, their emission can be modelled as instantaneous. It is shown in Gessey-Jones et al. (2022, see their table 1 and fig. B1) for NR Pop III stars that adopting the instantaneous emission approximation has negligible impact on the 21-cm

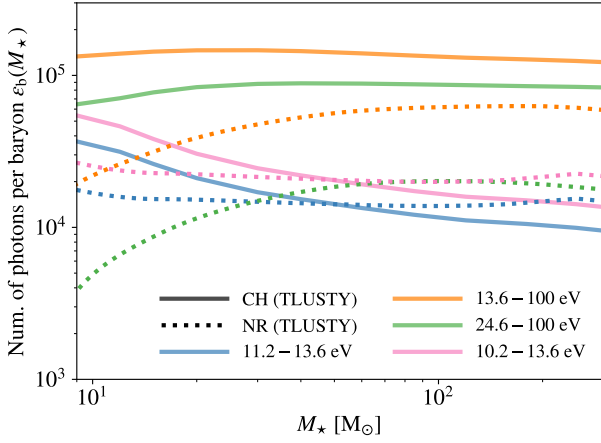


Figure 3. Number of photons emitted per stellar baryon $\epsilon_b(M_\star)$ during MS as a function of stellar mass M_\star based on TLUSTY stellar atmosphere models in 4 bands: LW (11.2 – 13.6 eV, blue), ionizing radiation for hydrogen (13.6 – 100 eV, orange) and helium (24.6 – 100 eV, green), and Lyman-band (10.2 – 13.6 eV, pink). The results for CH and NR stars are shown with solid and dotted curves, respectively. The latter are derived from the spectra in Gessey-Jones et al. (2022).

signal when the Pop III IMF is dominated by short-lived ($\lesssim 30$ Myr) massive stars. We have verified by numerical experiments that this is also the case for our CH Pop III stars. Therefore, now we focus on the MS lifetime-integrated spectrum $\epsilon(\nu; M_\star) = \int_0^{t_{\text{MS}}} L_\nu(t) dt$ to demonstrate the difference between CH and NR Pop III stars, given the specific luminosity $L_\nu(t)$. Fig. 2 shows the spectra for CH Pop III stars with $M_\star = 9, 40, 120$ and $300 M_\odot$ in comparison with those for NR Pop III stars based on linear interpolation of the spectra from Gessey-Jones et al. (2022) in the $\log \epsilon$ - $\log M_\star$ space. We find that CH stars have harder spectra due to their compact, hot nature, with boosted emission of ionizing photons, especially for relatively small stars. For both CH and NR Pop III stars, the Lyman-band continuum is almost flat (see the lower panel in Fig. 2), which is enhanced by CHE for $M_\star \lesssim 50 M_\odot$ but reduced for $M_\star \gtrsim 50 M_\odot$. The trend at $M_\star \gtrsim 50 M_\odot$ is caused by the fact that massive stars under CHE are so hot that they primarily produce more energetic (ionizing) photons and less Lyman-band photons.

To better quantify the difference made by CHE, we calculate the number of photons emitted per stellar baryon (i.e., emission efficiency) during MS as a function of M_\star :

$$\epsilon_b(M_\star) = (m_{\text{H}}/M_\star) \int_{\nu_1}^{\nu_2} \epsilon(\nu; M_\star) d\nu, \quad (1)$$

where ν_1 and ν_2 define the frequency range of the band of interest, and m_{H} is proton mass. We consider 4 representative bands relevant for reionization and the 21-cm signal (see Sec. 3): Lyman-band (10.2 – 13.6 eV), Lyman-Werner (LW, 11.2 – 13.6 eV), hydrogen (13.6 – 100 eV) and helium first (24.6 – 100 eV) ionizing photons. Our analysis is restricted to UV photons below 100 eV because the number of more energetic photons is negligible. In Fig. 3 we compare the results for CH Pop III stars and those for NR Pop III stars (Gessey-Jones et al. 2022). According to TLUSTY results + extrapolation, with CHE, the emission efficiency of LW photons $\epsilon_b^{\text{LW}}(M_\star)$ decreases with increasing M_\star , while $\epsilon_b^{\text{Ly}}(M_\star) \sim 1.5 \times 10^4$ is almost constant for $M_\star \sim 9 - 300 M_\odot$ in the NR case. It turns out that $\epsilon_b^{\text{Ly}}(M_\star)$ is enhanced by CHE for $M_\star \lesssim 50 M_\odot$ by up to a factor of 2 at $M_\star = 9 M_\odot$ but reduced for $M_\star \gtrsim 50 M_\odot$ by up to 36% at

$M_\star = 300 M_\odot$. The results for the full Lyman band are similar to those for LW photons. On the other hand, the production of ionizing photons is significantly enhanced with CHE across the mass range considered here, by a factor of $\sim 2 - 6$ and $\sim 3 - 14$ for hydrogen and helium first ionization, respectively. The boost is stronger for more energetic photons and less massive stars. We compare our results based on TLUSTY with those from black-body spectra in Appendix B, which shows that the black-body approximation causes non-negligible errors in $\epsilon_b(M_\star)$ by up to a factor of a few, although the general trends still hold.

3 SEMI-NUMERICAL SIMULATIONS OF COSMIC DAWN AND EOR

We use the semi-numerical code 21cmSPACE (e.g., Visbal et al. 2012; Fialkov et al. 2012) to simulate the 21-cm signal and ionization history of the IGM at $z \geq 6$. In this section, we briefly summarize the key physical elements in our numerical framework particularly focusing on the prescription for IGM ionization by stellar UV radiation, which is updated to self-consistently capture the effects of CH/NR Pop III stars and photo-heating feedback by IGM ionization (Sec. 3.2). The reader is referred to Gessey-Jones et al. (2022, see their sec. 4) and Gessey-Jones et al. (2023, see their sec. 3.1, 3.2, and references therein) for more detailed descriptions of the implementations of the relevant physics.

3.1 Theoretical background of the 21-cm signal

The 21-cm signal is produced by the absorption or emission at the 21-cm spectral line ($\nu_{21} = 1420$ MHz) of hydrogen atoms via transitions between hyper-fine states. It is measured by the differential 21-cm brightness temperature seen by an observer at $z = 0$:

$$T_{21}(\nu) = (1 - e^{-\tau_{21}}) \frac{T_S(z) - T_\gamma(z)}{(1+z)}, \quad (2)$$

which denotes the difference in radiation temperature at the observer-frame frequency $\nu = \nu_{21}/(1+z)$ caused by IGM absorption/emission at redshift z , given the radio background temperature $T_\gamma(z)$ at ν_{21} . Here $T_S(z)$ is the spin temperature that reflects the occupation fractions of hydrogen hyper-fine states, and τ_{21} is the 21-cm optical depth (Madau et al. 1997; Barkana 2016):

$$\tau_{21}(z) = \frac{3hc^3 A_{10}}{32\pi k_{\text{B}} \nu_{21}^2} \frac{x_{\text{HI}}(z) n_{\text{HI}}(z)}{(1+z)(d\nu_{\parallel}/dr_{\parallel})} \frac{1}{T_S(z)}, \quad (3)$$

where $A_{10} = 2.85 \times 10^{-15} \text{ s}^{-1}$ is the spontaneous emission rate of the 21-cm transition, $d\nu_{\parallel}/dr_{\parallel} \sim H(z)/(1+z)$ is the proper velocity gradient along the line of sight caused by cosmic expansion given the Hubble parameter $H(z)$, $n_{\text{HI}}(z)$ is the physical number density of hydrogen nuclei, and $x_{\text{HI}}(z)$ is the neutral fraction. For simplicity, we assume that T_γ is the radiation temperature of the cosmic microwave background (CMB) as $T_\gamma(z) = 2.725(1+z)$ K (see, e.g., Ewall-Wice et al. 2018; Feng & Holder 2018; Fialkov & Barkana 2019; Reis et al. 2020 for models of excess radio backgrounds).

Clearly, the 21-cm signal is sensitive to the redshift evolution of T_S , x_{HI} , and n_{HI} in the IGM, which are regulated by cosmic structure formation, star formation, and radiation transfer. In particular, the spin temperature T_S is determined by three processes: CMB scattering, atomic collisions, and Ly α scattering, i.e., the Wouthuysen–Field (WF) effect (Wouthuysen 1952; Field 1958). The strengths of these processes are denoted by the corresponding coupling coefficients,

x_γ , x_c , and x_α derived from atomic physics. In the end, T_S can be written as (Barkana 2016)

$$T_S^{-1} = \frac{x_\gamma T_\gamma^{-1} + x_c T_K^{-1} + x_\alpha T_C^{-1}}{x_\gamma + x_c + x_\alpha}. \quad (4)$$

Here, T_K is the kinetic temperature of the IGM, and T_C is the colour temperature of Ly α radiation (Madau et al. 1997; Barkana 2016). In the neutral IGM before reionization that is highly opaque to resonant scattering of Ly α photons, T_C is very close to T_K (Field 1959). A variety of processes are considered to drive the evolution of T_K (see eq. 13 in Gessey-Jones et al. 2023), including cosmic expansion, structure formation, ionization, X-ray heating, Compton heating, and Ly α heating (e.g., Madau et al. 1997; Fialkov et al. 2014b; Reis et al. 2021).

Shortly after the onset of first star formation, the UV radiation from Pop III stars is expected to make the WF effect dominant over the other processes, leading to $T_S \approx T_K$. The relevant coupling coefficient x_α is proportional to the intensity J_α of Ly α photons. Following the methodology of Reis et al. (2021) as an extension of Barkana & Loeb (2005) and Fialkov et al. (2014a), J_α is calculated by convolving radiation transfer window functions with the Lyman-band emissivity fields in our simulations, which are then derived from the spectra and star formation histories of individual stellar populations (Gessey-Jones et al. 2023, see their eq. 14 and the following text). For the Pop III emissivity field, we follow the method in Gessey-Jones et al. (2022), integrating the spectra of individual stars (Fig 2) over the IMF, which is assumed to follow a power-law form $dN/dM_\star \propto M_\star^{-\alpha}$ in a fixed range $M_\star \in [9, 300] M_\odot$ for both NR and CH stars. We consider 3 values of the slope $\alpha = 0, 1, \text{ and } 2.35$ to explore the effects of IMF. The star formation histories of Pop III and II stars are also used to model IGM ionization, as discussed below.

3.2 Updated prescription for IGM ionization

We derive the IGM neutral fraction x_{HI} of each cell in the simulation box under the assumption that (1) the ionization from stellar UV radiation takes the form of fully ionized bubbles, while (2) other sources of ionization (e.g., X-rays) can travel long distances in the IGM to cause partial ionization. For the former process, the excursion set formalism (Furlanetto et al. 2004; Mesinger et al. 2011) is used to identify fully ionized regions: a cell at position \mathbf{x} is fully ionized, i.e., $x_{\text{HI}}(\mathbf{x}) = 0$, if there exists a spherical volume of radius R centred on it in which the time-integrated (effective) number of ionizing UV photons exceeds the number of neutral atoms, i.e.

$$\exists R < R_{\text{max}}, \quad \text{so that} \quad n_{\gamma, \text{ion}}(\mathbf{x}, R) > 1 - x_{e, \text{oth}}(\mathbf{x}, R), \quad (5)$$

where R_{max} is the maximum radius of ionized bubbles, $n_{\gamma, \text{ion}}(\mathbf{x}, R)$ is the cumulative effective number of ionizing photons per baryon averaged over a sphere of radius R centred on \mathbf{x} , and $x_{e, \text{oth}}(\mathbf{x}, R)$ is the partially ionized fraction caused by long-range agents (2) averaged over the same sphere, which is evolved using eq. 17 in Gessey-Jones et al. (2023). We adopt $R_{\text{max}} = 50$ cMpc motivated by theoretical predictions and observations of the mean free path of ionizing photons at the end of reionization ($z \sim 5 - 6$, Wyithe & Loeb 2004; Furlanetto & Oh 2005; Lewis et al. 2022; Zhu et al. 2023).

If the criterion in Eq. 5 is never satisfied down to the resolution (i.e., cell size Δx) of the simulation, the ionized bubble is confined in the cell. In this case, the cell is treated as a two-phase medium, one fully ionized with a volume occupation fraction of $n_{\gamma, \text{ion}}(\mathbf{x})$ and one ionized to $x_{e, \text{oth}}(\mathbf{x})$, which is an approximation validated by Zahn

et al. (2011). The overall neutral fraction is then calculated locally as

$$x_{\text{HI}}(\mathbf{x}) = 1 - n_{\gamma, \text{ion}}(\mathbf{x}) - [1 - n_{\gamma, \text{ion}}(\mathbf{x})]x_{e, \text{oth}}(\mathbf{x}). \quad (6)$$

Here, following previous studies (Fialkov & Barkana 2014; Fialkov et al. 2017; Gessey-Jones et al. 2023), the single ionization fractions of hydrogen and helium are assumed to be identical, and helium double ionization in the IGM is not modelled in the simulation, which is expected to be driven by active galactic nuclei at relatively low redshifts $z \sim 3 - 6$ (Götberg et al. 2020, see their fig. 8) beyond the scope of this paper¹³. Besides, we assume that once a region is fully ionized, it remains ionized thereafter. That is to say, ionized bubbles are not allowed to shrink by recombination in our simulations although this may happen in reality if the UV emissivity declines, which can even cause non-monotonic evolution of the cosmic average neutral fraction (Salvador-Solé et al. 2017, 2022). We defer a more comprehensive model for the dynamical balance between ionization and recombination to future work.

In this work, we introduce a new scheme to calculate $n_{\gamma, \text{ion}}(\mathbf{x}, R)$ considering the Pop III and II contributions separately. This is an improvement over Gessey-Jones et al. (2023) in which $n_{\gamma, \text{ion}}(\mathbf{x}, R)$ is associated to the fraction of baryons collapsed into galaxies using a phenomenological efficiency parameter ζ without distinguishing Pop III and II stars. To be specific, we have

$$n_{\gamma, \text{ion}}(\mathbf{x}, R) = \min[1, n_{\gamma, \text{ion, II}}(\mathbf{x}, R) + n_{\gamma, \text{ion, III}}(\mathbf{x}, R)], \quad (7)$$

$$n_{\gamma, \text{ion, } i}(\mathbf{x}, R) \equiv \frac{\mu \epsilon_{b, i}^{\text{ion}} f_{\text{esc}, i} f_{\text{stellar}, i}(\mathbf{x}, R)}{(1 + N_{\text{rec}})}, \quad i = \text{II}, \text{III},$$

where N_{rec} is the average number of recombinations experienced per baryon before remaining ionized (which captures the effects of IGM clumping and attenuation), $f_{\text{stellar}, i}(\mathbf{x}, R)$ is the fraction of *all* baryons that have formed Pop i stars¹⁴, and $\epsilon_{b, i}^{\text{ion}}$ and $f_{\text{esc}, i}$ are the corresponding (IMF-averaged) number of ionizing photons produced per stellar baryon and escape fraction. We calculate $f_{\text{stellar}, i}$ by integrating the star formation rate density (SFRD) $\dot{\rho}_{\star, i}$:

$$f_{\text{stellar}, i}(\mathbf{x}, R, z) = \frac{\int_z^{z_{\text{ini}}} \dot{\rho}_{\star, i}(\mathbf{x}, R, z') |dt/dz'| dz'}{\rho_b(\mathbf{x}, R, z)}, \quad i = \text{II}, \text{III}, \quad (8)$$

where $z_{\text{ini}} = 50$ is the initial redshift of the simulation and $\rho_b(\mathbf{x}, R, z)$ is the baryon density. Note that all the quantities involved in Eqs. 7 and 8 are averaged over spherical volumes in the excursion-set formalism (Eq. 5).

The SFRD in each cell plays a crucial role in the above calculation. For cells that are not fully ionized by UV radiation, we treat the contributions from fully ionized and partially ionized regions differently, which are then combined with the weights $n_{\gamma, \text{ion}}$ (ionized fraction of the cell) and $1 - n_{\gamma, \text{ion}}$. For Pop III stars, we estimate the SFRD under the assumption that Pop III stars only form in one burst (per halo) once the halo crosses a mass threshold M_{min} , which is set to the minimum of the critical masses for efficient molecular (M_{mol}) and atomic cooling (M_{atm}), i.e.,

¹³ In primordial nebulae hosting massive Pop III stars, helium double ionization can be efficient locally due to the hard stellar spectra, which powers strong HeII $\lambda 1640\text{\AA}$ lines as a key signature of Pop III star formation (e.g., Bromm et al. 2001; Venditti et al. 2024; Lecroq et al. 2025). However, the number of helium doubly ionizing photons from Pop III stars is too low to have a strong effect on cosmic reionization even under CHE (Sibony et al. 2022).

¹⁴ Note that f_{stellar} and f_\star are distinct. The latter generally describes the fraction of gas in *star-forming halos* that become stars (SFE), while f_{stellar} is defined for *all* baryons including those not in star-forming haloes.

$M_{\min} = M_{\text{cool}} \equiv \min(M_{\text{mol}}, M_{\text{atm}})$ (Magg et al. 2022a). Here, $M_{\text{mol}} = M_{z=20} f_{\text{LW}} f_{\text{vbc}} [(1+z)/21]^{-3/2}$ with suppression factors for LW feedback (f_{LW}) and streaming motion (f_{vbc}) given by the simulation-motivated fitting formula detailed in Muñoz et al. (2022, see their sec. 2.2.2). We adopt $M_{z=20} = 5.8 \times 10^5 M_{\odot}$ (Schauer et al. 2021) and $M_{\text{atm}} = 10^8 M_{\odot} [V_{\text{c,atm}}/(17 \text{ km s}^{-1})]^3 [(1+z)/10]^{-3/2}$ given $V_{\text{c,atm}} = 16.5 \text{ km s}^{-1}$, which is the circular velocity of critical atomic-cooling haloes (Gessey-Jones et al. 2022). For simplicity, Pop III star formation is forbidden in fully ionized regions (i.e., fully ionized cells and UV-ionized bubbles in partially ionized cells), since haloes massive enough ($\gtrsim 10^9 M_{\odot}$) to overcome photo-heating feedback (see below) are typically metal-enriched and no longer form Pop III stars (see, e.g., figs. 6 and 9 in Ventura et al. 2023)¹⁵. In this way, the Pop III SFRD in a cell at cosmic age t is given by

$$\dot{\rho}_{\star, \text{III}}(t) = \frac{f_{\star, \text{III}}(1 - n_{\gamma, \text{ion}})}{\Delta t_{\star, \text{III}}} \max \left\{ 0, M_{\min}(t) \times \int_{M_{\min}(t)}^{M_{\max}} \left[\frac{d\rho_{\text{g}}(t + 0.5\Delta t_{\star, \text{III}})}{dM'} - \frac{d\rho_{\text{g}}(t - 0.5\Delta t_{\star, \text{III}})}{dM'} \right] \frac{dM'}{M'} \right\}. \quad (9)$$

Here $d\rho_{\text{g}}/dM' \equiv f_{\text{b}} M' dn_{\text{h}}/dM'$ is the baryon density per unit halo mass, given the halo mass function dn_{h}/dM' (number density of haloes per unit mass) and the baryon fraction f_{b} in a halo as functions of t and M' , which also depend on the overdensity δ and relative velocity v_{bc} between baryons and dark matter¹⁷ in the cell (Tseliakhovich & Hirata 2010; Barkana & Loeb 2011; Naoz et al. 2011, 2013; Fialkov et al. 2012), $f_{\star, \text{III}}$ is the average Pop III SFE (i.e., mass fraction of baryons in Pop III star-forming haloes that become stars), $M_{\max} = 10^{12} M_{\odot}$ is the upper bound of halo mass chosen to cover most halos at $z \gtrsim 6$, and $\Delta t_{\star, \text{III}} = 2 \text{ Myr}$ is a characteristic timescale chosen to be marginally below the lifetimes of most Pop III stars with initial masses $M_{\star} \lesssim 300 M_{\odot}$.

For Pop II stars that can form continuously in metal-enriched haloes, we instead use the following formula for both neutral and ionized regions as an extension of the model in Park et al. (2019):

$$\dot{\rho}_{\star, \text{II}}(t) = \frac{f_{\star, \text{II}} f_{\text{II}}(t)}{t_{\star, \text{II}} H(t)^{-1}} \int_{M_{\min}(t)}^{M_{\max}} f_{\text{sup}}(M') \frac{d\rho_{\text{g}}(t)}{dM'} dM'. \quad (10)$$

Here $f_{\star, \text{II}}$ is the average Pop II SFE, $t_{\star, \text{II}} = 0.2$ is chosen such that $t_{\star, \text{II}} H(t)^{-1}$ approximately corresponds to the characteristic dynamical time of a halo (Reis et al. 2022), $f_{\text{sup}}(M') = \log(M'/M_{\min})/\log(M_{\text{atm}}/M_{\min})$ is a suppression factor that captures the reduction of gas mass available for Pop II star formation in haloes below the atomic-cooling threshold M_{atm} (Fialkov et al. 2013, note that $f_{\text{sup}} = 1$ for $M' \geq M_{\text{atm}}$)¹⁸, and $f_{\text{II}}(t)$ is the mass fraction

of star-forming haloes that host Pop II stars, which is a function of δ and v_{bc} , given by fits to the results in Magg et al. (2022a) for the transition from Pop III to Pop II star formation derived from halo merger trees using the semi-analytical code *A-SLOTH* (Hartwig et al. 2022, 2024). In Magg et al. (2022a), f_{II} also depends on the recovery time t_{rec} that describes how fast a halo can restore its gas reservoir for star formation after the SN explosions of the first generation of stars. We explore the impact of t_{rec} on our results considering three values $t_{\text{rec}} = 10, 30, \text{ and } 100 \text{ Myr}$. In neutral regions we set the halo mass threshold as $M_{\min} = M_{\text{cool}}$, while in fully ionized regions, we further consider the lower limit M_{crit} (above which gas can still cool to form stars under the irradiance of UV fields in ionized bubbles) imposed by photo-heating/ionization feedback (Sobacchi & Mesinger 2013, see their eq. 3) following Cohen et al. (2016), such that $M_{\min} = \max(M_{\text{cool}}, M_{\text{crit}})$.

To evaluate Eqs. 7-10, for Pop III stars we adopt a typical escape fraction $f_{\text{esc, III}} = 0.5$ based on the 1D radiation transfer calculations in Sibony et al. (2022), which is also close to the best-fitting value $f_{\text{esc, III}} = 0.525$ inferred from observations with *A-SLOTH* (Hartwig et al. 2024). $\epsilon_{\text{b, III}}^{\text{ion}}$ is derived self-consistently by averaging the production efficiency of ionizing photons as a function of M_{\star} (Fig. 3) over the IMF (weighted by M_{\star}). We vary the average Pop III SFE in the typical range $f_{\star, \text{III}} \in [10^{-4}, 0.01]$ predicted by analytical models and simulations of Pop III star formation (e.g., Hirano et al. 2023; Liu et al. 2024b). For Pop II stars, we fix the average SFE to $f_{\star, \text{II}} = 0.01$, which is chosen to reproduce the SFRD measured by galaxy surveys at $z \sim 6$ (e.g., Madau & Dickinson 2014; Finkelstein 2016; Algera et al. 2023; Donnan et al. 2023; Harikane et al. 2023; Robertson et al. 2024). To remain connected to the convention used in previous studies, we define a phenomenological ionization efficiency parameter for Pop II stars as $\zeta_{\text{II}} \equiv \mu \epsilon_{\text{b, II}}^{\text{ion}} f_{\star, \text{II}} f_{\text{esc, II}} / (1 + N_{\text{rec}})$, so the Pop II contribution in Eq. 7 can be written as $n_{\gamma, \text{ion, II}} = \zeta_{\text{II}} f_{\text{coll}}$, where $f_{\text{coll}} \equiv f_{\text{stellar, II}}/f_{\star, \text{II}}$ is the cumulative mass fraction of baryons that constitute the gas reservoir for Pop II star formation, and $\mu \sim 1.22$ is the mean molecular weight of neutral IGM. We adopt a conservative value $\zeta_{\text{II}} = 4$ given $f_{\star, \text{II}} = 0.01$, $\epsilon_{\text{b, II}}^{\text{ion}} = 1.3 \times 10^4$ corresponding to a stellar population¹⁹ with a Kroupa (2001) IMF from 0.1 to $300 M_{\odot}$ and metallicity of $Z = 0.0004$, $f_{\text{esc, II}} = 0.1$, a typical value inferred from observations at $z \sim 2 - 12$ (Mitra & Chatterjee 2023; Asthana et al. 2024), and $N_{\text{rec}} = 3$ based on observations of the mean free path of ionizing photons (which imply $N_{\text{rec}} + 1 \sim 3 - 6$, Davies et al. 2021, 2024). Here N_{rec} is fixed for simplicity. We plan to consider the spatial and time evolution of N_{rec} with more self-consistent treatments of IGM clumping and attenuation in future work (see, e.g., Davies & Furlanetto 2022).

3.3 Cosmic structure formation and simulation setup

As cosmic structure formation sets the stage of IGM evolution, the overdensity δ and baryon-dark matter relative velocity v_{bc} fields together with the initial IGM properties at $z_{\text{ini}} = 50$ serve as the foundations of our simulations through their impact on ρ_{b} , $d\rho_{\text{g}}/dM'$, M_{\min} , and f_{II} . In this study, these fields are created on a 128^3 grid cubic cells with a cell size of 3 cMpc. Structure formation remains

factor $f_{\text{sup}}(M')$ is introduced via a halo mass-dependent SFE $f_{\star}(M') \equiv f_{\star, \text{II}} f_{\text{sup}}(M')$.

¹⁹ We extrapolate the fitting formulae for the production rate of ionizing photons and lifetime as functions of initial stellar mass from Schaefer (2002, see their table 6) to derive $\epsilon_{\text{b, II}}^{\text{ion}}$.

¹⁵ Some cosmological simulations found that Pop III star formation can still occur in pockets of pristine gas in massive haloes under inhomogeneous metal enrichment (e.g., Tornatore et al. 2007; Xu et al. 2016; Benitez-Llambay & Frenk 2020; Liu & Bromm 2020b; Venditti et al. 2023). How much this scenario contributes to the overall Pop III SFRD is still uncertain as metal mixing is poorly understood.

¹⁶ The overdensity δ (on the scale of 3 cMpc corresponding to the spatial resolution of simulations) is defined such that the local baryon density follows $\rho_{\text{b}} = (1 + \delta)\bar{\rho}_{\text{b}}$ given the cosmic average baryon density $\bar{\rho}_{\text{b}}$. Similarly, we have $n_{\text{H}} = (1 + \delta)X_{\text{p}}\bar{\rho}_{\text{b}}/m_{\text{H}}$, where $X_{\text{p}} = 0.76$ is the primordial hydrogen mass fraction, and m_{H} is proton mass.

¹⁷ Structure formation and collapse of gas into haloes are regulated by the relative velocity (i.e., streaming motion) between baryon and dark matter, whose density fluctuations are different at small-scales, such that the halo baryon fraction is lower than the cosmic average value $f_{\text{b}, 0} = \Omega_{\text{b}}/\Omega_{\text{m}} \approx 0.16$ (Planck Collaboration 2020) in small haloes.

¹⁸ In the original terminology of Fialkov et al. (2013), the suppression

Table 1. Simulation parameters. The first section shows the parameters fixed throughout this work. The second section shows the parameters that are explored in physically motivated ranges.

Symbol	Value(s)/range	Definition
$f_{\star, \text{II}}$	0.01	Average Pop II star formation efficiency
$t_{\star, \text{II}}$	0.2	Pop II star formation timescale parameter
ζ_{II}	4	Pop II ionization efficiency
$f_{\text{X, II}}$	1	Pop II galactic X-ray emission efficiency
$f_{\text{X, III}}$	0	Pop III galactic X-ray emission efficiency
α_{X}	-1.5	Power-law slope of the X-ray spectrum
$E_{\text{X, min}}$	0.1 keV	Lower energy bound of X-ray photons
N_{rec}	3	Number of recombinations per baryon
R_{max}	50 cMpc	Maximum ionized bubble radius
M_{min}	9 M_{\odot}	Minimum Pop III mass
M_{max}	300 M_{\odot}	Maximum Pop III mass
$f_{\text{esc, III}}$	0.5	Escape fraction of Pop III ionizing photons
$M_{z=20}$	$5.8 \times 10^5 M_{\odot}$	Minimum mass of molecular-cooling haloes with Pop III star formation at $z = 20$
$f_{\star, \text{III}}$	$10^{-4} - 0.01$	Average Pop III star formation efficiency
α	0, 1, 2.35	Slope of Pop III IMF: $\frac{dN}{dM_{\star}} \propto M_{\star}^{-\alpha}$
t_{rec}	10, 30, 100	Recovery time [Myr] from Pop III SNe

marginally linear at scales larger than the cell size for $z \geq 6$. Therefore, the overdensity field is evolved in a self-similar manner from the initial condition δ_{ini} as $\delta(z) = D(z)\delta_{\text{ini}}$, where $D(z)$ is the normalized growth factor ($D(z_{\text{ini}}) = 1$) obtained by solving the linear perturbation equations (e.g., Mo et al. 2010), v_{bc} simply decays with time as $v_{\text{bc}}(z) \propto (1+z)$, and the halo mass function and baryon fraction are calculated analytically in each cell following Barkana & Loeb (2004); Fialkov et al. (2012). The initial conditions for the fields of δ and v_{bc} are computed using CAMB (Lewis et al. 2000; Lewis & Bridle 2002; Lewis & Challinor 2011), while the initial IGM temperature and residual ionized fraction fields are calculated with RECFAST (Seager et al. 1999, 2011).

The impact of XRBs is modelled with a dimensionless parameter f_{X} that relates the X-ray luminosity L_{X} of a galaxy to the star formation rate (SFR): $L_{\text{X}} = 3 \times 10^{40} f_{\text{X}} \text{ erg s}^{-1} \times \text{SFR} / (M_{\odot} \text{ yr}^{-1})$. Given f_{X} , the X-ray emissivity can be easily derived from the SFRD (Eqs. 9 and 10). Throughout this paper, we adopt a typical value $f_{\text{X, II}} = 1$ for Pop II stars based on binary population synthesis predictions (e.g., Fragos et al. 2013a,b; Liu et al. 2024a) and observations in X-rays and radio (e.g., HERA Collaboration 2022; Bevins et al. 2023; Lehmer et al. 2022; Riccio et al. 2023; Dhandha et al. 2025). The X-ray spectrum is assumed to be a power law with a slope of $\alpha_{\text{X}} = -1.5$ and lower photon energy bound of 0.1 keV (Fialkov et al. 2014b, 2017). The Pop III contribution is simply ignored with $f_{\text{X, III}} = 0$ because our focus is the effects of UV radiation, and Pop III XRBs are poorly understood due to the absence of direct observations and large uncertainties in binary population synthesis models of Pop III stars (Ryu et al. 2016; Liu et al. 2021a; Sartorio et al. 2023, see, e.g.,).

As mentioned in the previous subsections, the underlying/initial fields are combined with parameterized prescriptions for star formation, stellar emission, and radiation transfer to evolve the state of the IGM. The parameters that are most relevant for this work are listed in Table 1, which are assumed to be constant throughout the simulation box and time-span for simplicity. In reality, these parameters can have non-trivial (even stochastic) time evolution, dependence on halo properties (e.g., Tacchella et al. 2018; Qin et al. 2020; Cohen et al. 2017; Muñoz et al. 2022; Kaur et al. 2022; Sibony et al. 2022;

Table 2. IMF-averaged emission efficiency (number of photons emitted per stellar baryon) of Pop III stars in different bands. Column 1 is the Pop III IMF slope α ($dN/dM_{\star} \propto M_{\star}^{-\alpha}$). Columns 2, 4, and 6 show the results for (hydrogen) ionizing photons (13.6 – 100 eV), Lyman-band photons (10.2 – 13.6 eV), and LW photons (11.2–13.6 eV), respectively, from CH Pop III stars, while Columns 3, 5, and 7 show the results from their NR counterparts.

α	$\epsilon_{\text{b, III}}^{\text{ion}}$ (CH)	$\epsilon_{\text{b, III}}^{\text{ion}}$ (NR)	$\epsilon_{\text{b, III}}^{\text{Ly}}$ (CH)	$\epsilon_{\text{b, III}}^{\text{Ly}}$ (NR)	$\epsilon_{\text{b, III}}^{\text{LW}}$ (CH)	$\epsilon_{\text{b, III}}^{\text{LW}}$ (NR)
2.35	138972	45882	28251	21908	19449	14952
1	131015	59063	17376	21166	12108	14583
0	127394	61140	15224	21407	10635	14742

Harikane et al. 2023; Kim et al. 2024; Asthana et al. 2024), and spatial fluctuations (e.g., Cohen et al. 2018; Reis et al. 2022). Among these parameters, we particularly focus on the average SFE $f_{\star, \text{III}}$ and IMF slope α of Pop III stars, and the recovery time t_{rec} for Pop II star formation, which are varied in reasonable ranges motivated by the typical values from analytical models and hydrodynamic simulations of Pop III star formation (e.g., Hirano et al. 2014, 2015, 2023; Klessen & Glover 2023; Liu et al. 2024b) and Pop II star formation in haloes enriched by Pop III SNe (e.g., Jeon et al. 2014; Smith et al. 2015; Chiaki et al. 2018; Chiaki & Wise 2019; Latif & Schleicher 2020; Abe et al. 2021; Magg et al. 2022b; Chen et al. 2024; Hartwig et al. 2024). The other parameters are fixed for simplicity. We also do not consider any correlations between parameters that may exist in reality²⁰. Throughout this paper, we assume the standard Λ CDM cosmology and use the best-fitting cosmological parameters from Planck Collaboration et al. (2014, see the best-fit results for *Planck*+WP in their table 2): $\Omega_{\text{m}} = 0.3183$, $\Omega_{\text{b}} = 0.0490$, $H_0 = 67.04 \text{ km s}^{-1} \text{ Mpc}^{-1}$, $\sigma_8 = 0.8347$, and $n_{\text{s}} = 0.9619$.

4 RESULTS

In this section, we compare the results for CH and NR Pop III stars under different choices of $f_{\star, \text{III}}$, α , and t_{rec} , in terms of the cosmic star formation history (Sec. 4.1), reionization (Sec. 4.2), and 21-cm signal (Sec. 4.3). Focusing on the differences between NR and CH stellar evolution, we only consider two extreme cases in which *all* Pop III stars are either NR or CH throughout their MS, although a realistic Pop III population can be a mixture of stars in different evolution pathways (see, e.g., Liu et al. 2025). The exact fraction of stars with CHE is determined by the initial distribution of spins, mass transfer processes in binaries, and detailed mixing mechanisms of achieving CHE (see, e.g., Maeder & Meynet 2000; Yoon et al. 2006; Brott et al. 2011; Szécsi et al. 2015; Ghodla et al. 2022; Dall’Amico et al. 2025), which are still poorly understood. We define $f_{\star, \text{III}} = 0.003$, $\alpha = 1$, and $t_{\text{rec}} = 30 \text{ Myr}$ as the fiducial model. Among these three key parameters, we vary one parameter at a time while keeping the rest fixed to the fiducial choices. The other parameters governing the UV and X-ray emission from Pop II stars are always fixed (see the first section of Table 1). To better interpret the results, we calculate the IMF-averaged emission efficiency of Pop III stars for three representative bands, as shown in Table 2.

²⁰ It is shown in Sibony et al. (2022) that $f_{\text{esc, III}}$ increases with higher $f_{\star, \text{III}}$, a more top-heavy IMF, or CHE.

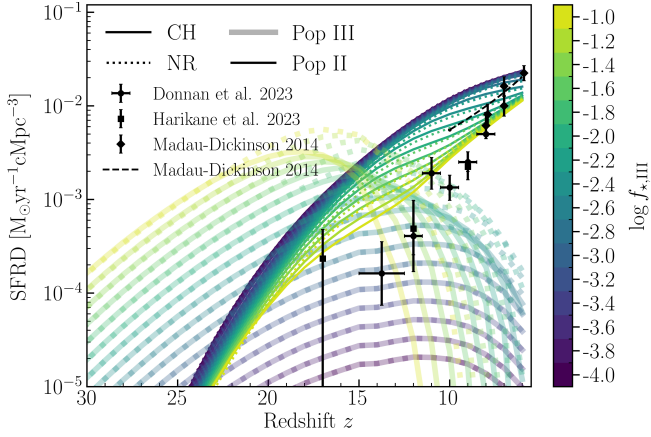


Figure 4. Cosmic SFRD for Pop III (thick curves) and Pop II (thin curves) stars from our simulations using the NR (dotted) and CH (solid) Pop III stellar evolution models. The Pop III SFE is varied in the range $f_{\star,III} = 10^{-4} - 0.01$ with fixed $\alpha = 1$ and $t_{\text{rec}} = 30$ Myr, where the results for higher $f_{\star,III}$ are denoted by lighter colours. For comparison, the data points with 1σ errorbars show the observational results for total/Pop II SFRD (Madau & Dickinson 2014; Donnán et al. 2023; Harikane et al. 2023) compiled by CoReCon (Garaldi 2023). The fit $\text{SFRD} = 0.015(1+z)^{2.7}/\{1 + [(1+z)/2.9]^{5.6}\} M_{\odot} \text{ yr}^{-1} \text{ Mpc}^{-3}$ from Madau & Dickinson (2014) is shown with the dashed line.

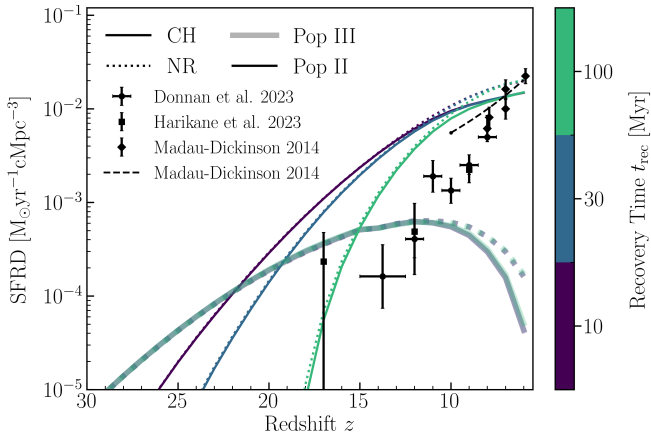


Figure 5. Same as Fig. 4 but varying the recovery time in the range $t_{\text{rec}} \sim 10 - 100$ Myr with fixed $\alpha = 1$ and $f_{\star,III} = 0.003$.

4.1 Star formation history

To justify the ranges of parameters explored (Table 1), we compare the predicted SFRD with that inferred from observations (Madau & Dickinson 2014; Donnán et al. 2023; Harikane et al. 2023) in Fig. 4 and 5, where $f_{\star,III}$ and t_{rec} are varied, respectively. The observational data are obtained from the python package CoReCon²¹ (Garaldi 2023). The effects of α on the SFRD are negligible and not shown. Cosmic star formation is always dominated by Pop II stars at $z \lesssim 15$ where observational results have 1σ errors less than 1 dex. Interestingly, the Pop II/total SFRD decreases with $f_{\star,III}$. This is caused by the suppression of star formation by photo-heating feedback in ionized regions (where M_{min} is higher, see Sec. 3.2) whose volume filling fraction is enhanced by higher $f_{\star,III}$ and CHE. The effect of $f_{\star,III}$ is stronger at lower z for $z \sim 20 - 12$ given $f_{\star,III} \gtrsim 0.001$ where

a significant fraction ($\gtrsim 0.1$) of the IGM has already been ionized by $z \sim 12$. It is also stronger in the CH case. This is a signature of *external* ionization feedback in which ionized bubbles powered by rapid star formation in over-dense regions expand to less dense regions that could not be ionized by local star formation. At $z \lesssim 12$, the results from different models tend to converge due to self-regulation of star formation by feedback. The Pop III SFRD is significantly reduced at late epochs under enhanced ionization feedback (by higher $f_{\star,III}$ and/or CHE), since Pop III star formation is forbidden in ionized regions.

For $f_{\star,III} \lesssim 0.001$ and/or at $z \sim 20 - 30$, the reduction of Pop II SFRD by higher $f_{\star,III}$ is almost independent of z but still non-negligible, which is instead driven by *local* ionization feedback. In this regime, the volume fraction of ionized regions remains small. However, as early star formation is highly clustered, favoring over-dense regions, it is spatially correlated with IGM ionization, which significantly enhances local ionization feedback²². Meanwhile, in these over-dense regions, the transition from Pop III to Pop II star formation is faster and nearly complete when local ionization feedback kicks in (see fig. 3 in Magg et al. 2022a). Therefore, the contribution of these regions to overall Pop III star formation is always small, such that the Pop III SFRD is insensitive to local reionization feedback, and remains almost proportional to $f_{\star,III}$.

It is shown in Fig. 5 that the Pop II SFRD is lower at $z \gtrsim 10$ with increasing t_{rec} , and effect is stronger at higher z . The difference between $t_{\text{rec}} = 10$ Myr and $t_{\text{rec}} = 100$ Myr exceeds one order of magnitude at $z \gtrsim 17$. However, the Pop III SFRD hardly varies, because it is only regulated by external ionization feedback at late epochs ($z \lesssim 10$ for $f_{\star,III} = 0.003$).

Our results for the total/Pop II SFRD are generally consistent with observations at $z \lesssim 7$, but the SFRD at higher redshifts is over-predicted by up to ~ 1 dex around $z \sim 14$. Since $f_{\star,II}$ is constant in our model, to match the observations at higher redshifts, one must increase t_{rec} and/or decrease $f_{\star,II}$ at the price of under-predicting the SFRD at lower redshifts where observational results are less uncertain. This implies that $t_{\text{rec}} \gtrsim 100$ Myr is favoured and/or our star formation model needs to be improved to fully reproduce observations, which is beyond the scope of this paper (see Dhandha et al. 2025)²³. Better agreements with observations can be achieved if the SFE decreases with halo mass in low-mass haloes, which is a natural consequence of stellar feedback and a common prescription in galaxy formation models (e.g., Tacchella et al. 2018; Behroozi et al. 2019; Shen et al. 2023). In our case with an optimistic constant value $f_{\star,II} = 0.01$ and the simulation-motivated choices of $t_{\text{rec}} \sim 10 - 100$ Myr, the contribution by Pop II stars is likely over-estimated at $z \gtrsim 7$. Therefore, the effects of Pop III stars (with respect to those of Pop II stars) in our simulations should be regarded as conservative estimates. Nevertheless, our Pop III star formation histories

²² Indeed, the UV radiation from one massive galaxy can significantly suppress star formation in nearby low-mass ($\lesssim 10^{9.5} M_{\odot}$) haloes (Zhu & Gao 2024).

²³ Note that the SFRD inferred from JWST observations (Donnán et al. 2023; Harikane et al. 2023) is derived by integrating the UV luminosity function up to the magnitude of $M_{\text{UV}} = -17$, which corresponds to $\text{SFR} \sim 0.3 M_{\odot} \text{ yr}^{-1}$ according to the canonical UV-SFR conversion coefficient (Madau & Dickinson 2014). However, the SFRD predicted by our simulations covers all galaxies, including those with $\text{SFR} \lesssim 0.3 M_{\odot} \text{ yr}^{-1}$. The contributions of such smaller galaxies can be large depending on the shape of the UV luminosity function, which may also explain the discrepancy. Better constraints on our simulation parameters can be obtained with the UV luminosity function itself rather than its integration, as shown in Dhandha et al. (2025)

²¹ <https://corecon.readthedocs.io/en/latest/index.html>

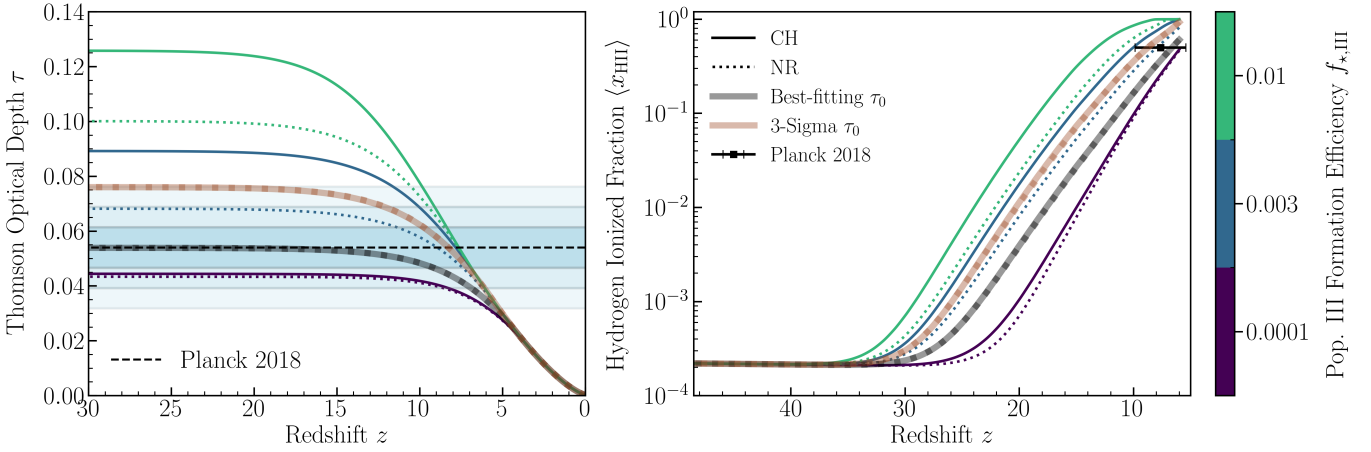


Figure 6. Ionization history in terms of the optical depth (left) and volume-averaged ionized fraction (right). The dotted (solid) curves show the results for the NR (CH) Pop III stellar evolution models, where the Pop III SFE is varied in the range $f_{\star,III} = 10^{-4} - 0.01$ (as marked on the colorbar) with fixed $\alpha = 1$ and $t_{\text{rec}} = 30$ Myr. Here, the results for higher $f_{\star,III}$ are denoted by lighter colours. In the left panel, the measurement of $\tau_0 \equiv \tau(z \rightarrow 1100)$ by Planck $\tau_0 = 0.0544 \pm 0.0073$ (Planck Collaboration 2020) is shown with the dashed line and shaded regions for $1 - 3\sigma$ errors. In the right panel, the error bar denotes the 3σ confidence interval of the redshift of instantaneous reionization $z_{\text{re}} = 7.67 \pm 0.73$ (when $\langle x_{\text{HII}} \rangle = 0.5$) inferred from observations (Planck Collaboration 2020). We also find the $f_{\star,III}$ values required to produce the best-fitting value $\tau_0 = 0.0544$ ($f_{\star,III} \sim 5.7 \times 10^{-4}$ and 1.3×10^{-3} for CH and NR stars) and the 3σ upper limit $\tau_0 = 0.0763$ ($f_{\star,III} = 1.8 \times 10^{-3}$ and 4.2×10^{-3} for CH and NR stars), as shown by the lower and upper thick curves, respectively.

are consistent with the predictions from previous analytical models and cosmological simulations (e.g., Johnson et al. 2013; de Souza et al. 2013, 2014; Smith et al. 2015; Xu et al. 2016; Mebane et al. 2018; Sarmento et al. 2017, 2018, 2019; Jaacks et al. 2018, 2019; Liu & Bromm 2020a,b; Dayal et al. 2020; Visbal et al. 2020; Skinner & Wise 2020; Hartwig et al. 2022; Muñoz et al. 2022; Venditti et al. 2023; Ventura et al. 2024). In particular, as shown below, we obtain a similar range of the cumulative stellar mass density (CSMD) of Pop III stars (ever formed) $\rho_{\star,III} \sim 10^4 - 10^6 M_{\odot} \text{Mpc}^{-3}$ as that covered by the above literature.

4.2 Ionization history

For simplicity, we characterize the progress of reionization with the global ionization history captured by the volume-averaged (hydrogen) ionized fraction $\langle x_{\text{HII}}(z) \rangle \equiv 1 - \langle x_{\text{HI}}(z) \rangle$ and the optical depth for Thomson scattering (Robertson et al. 2013; Hartwig et al. 2015):

$$\tau(z) = c\sigma_{\text{T}} \int_0^z f_{\text{e}} \langle x_{\text{HII}}(z') \rangle \bar{n}_{\text{H}}(z') dz' \quad (11)$$

given the cross-section of Thomson scattering σ_{T} , the cosmic average physical hydrogen number density $\bar{n}_{\text{H}}(z') \equiv X_{\text{p}} \bar{\rho}_{\text{b}}(z') / m_{\text{H}}$, and the number of free electrons per hydrogen nucleus $f_{\text{e}} = 1 + Y_{\text{p}} / (4X_{\text{p}})$, where $X_{\text{p}} = 0.76$ and $Y_{\text{p}} = 0.24$ are the primordial mass fractions of hydrogen and helium. Since our simulations stop at $z = 6$, we extrapolate $\langle x_{\text{HII}}(z) \rangle$ down to $z = 0$ as a linear function of $\log(1+z)$ (bounded by the lower limit 0). The contribution of helium double ionization is neglected for simplicity, which is expected to be small since helium double ionization can only increase f_{e} by up to $\sim 7\%$ reaching $f_{\text{e}} = 1 + Y_{\text{p}} / (2X_{\text{p}})$ at $z \lesssim 3$. The value $\tau_0 = 0.0544 \pm 0.0073$ measured from the CMB (Planck Collaboration 2020) is compared with our predictions for $\tau_0 \equiv \tau(z \rightarrow 1100)$ to put constraints on Pop III properties.

We find that the ionization history is mostly sensitive to $f_{\star,III}$ and the stellar evolution model adopted, while the effects of α and t_{rec} are minor (with small changes of $\Delta\tau_0 \lesssim 0.005$). Fig. 6 shows the results for the fiducial Pop III IMF ($\alpha = 1$) and recovery time ($t_{\text{rec}} = 30$ Myr) with varying Pop III SFE $f_{\star,III} \sim 10^{-4} - 0.01$. The results for varying

α and t_{rec} are shown in Appendix C. Reionization is accelerated by CHE and higher $f_{\star,III}$: $\langle x_{\text{HII}} \rangle$ is enhanced by a factor of ~ 2 at $z \sim 30 - 10$ in the CH models compared with their NR counterparts for $f_{\star,III} \gtrsim 0.001$. The impact of CHE is weaker for lower $f_{\star,III}$ and redshifts where Pop II stars dominate the ionization budget. In the extreme case with $f_{\star,III} = 0.01$, both CH and NR models are ruled out by observations. We find that $f_{\star,III} \approx 5.74 \times 10^{-4}$ and 1.28×10^{-3} are required for the CH and NR models to reproduce the best-fitting value of optical depth from Planck Collaboration (2020) $\tau_0 = 0.0544$, while $f_{\star,III} \approx 1.85 \times 10^{-3}$ (4.17×10^{-3}) leads to $\tau_0 = 0.0763$, the 3σ upper limit of τ_0 measured by Planck Collaboration (2020), in the CH (NR) model. This indicates that the ionization power of Pop III stars is boosted by a factor of ≈ 2 with CHE for a log-flat IMF in the range of $M_{\star} \in [9 - 300] M_{\odot}$. For all the models that satisfy $\tau_0 < 0.0763$, the Pop III contribution to τ is mostly achieved at $z \sim 8 - 15$, and the contribution from the earlier epoch ($z \gtrsim 15$) remains small ($\Delta\tau \lesssim 0.01$), below the upper limit of 0.02 from Planck Collaboration (2020), consistent with the findings in Muñoz et al. (2022).

To further quantify the contribution of Pop III stars to reionization, we derive the relation between τ_0 and the Pop III CSMD $\rho_{\star,III}$ through a series of simulations, as shown in see Fig. 7. For $\tau_0 < 0.0763$, we obtain a general linear relation (covering both CH and NR models):

$$\tau_0 \approx \tau_{\text{II}} + 0.0130 \left(\frac{f_{\text{esc},III}}{0.5} \right) \left(\frac{\epsilon_{\text{b},III}^{\text{ion}}}{10^5} \right) \left(\frac{\rho_{\star,III}}{10^5 M_{\odot} \text{Mpc}^{-3}} \right), \quad (12)$$

which is valid with relative errors in τ_0 less than $\sim 1\%$. Here, τ_{II} is the contribution to τ_0 by Pop II stars (corresponding to $f_{\star,III} \rightarrow 0$), and we have $\tau_{\text{II}} \approx 0.043$ for our choice of fiducial parameters $\zeta_{\text{II}} = 4$ and $t_{\text{rec}} = 30$ Myr. This linear relation (Eq. 12) provides similar constraints on Pop III star formation from reionization compared with the earlier results $\rho_{\star,III} \lesssim 10^4 - 10^6 M_{\odot} \text{Mpc}^{-3}$ in Visbal et al. (2015) and Inayoshi et al. (2016). For instance, $\tau_0 < 0.0763$ requires $\rho_{\star,III} \lesssim 2.0 (4.4) \times 10^5 M_{\odot} \text{Mpc}^{-3}$ for CH (NR) Pop III stars with $\alpha = 1$ and $\epsilon_{\text{b},III}^{\text{ion}} = 1.3 \times 10^5 (6.0 \times 10^4)$ given $f_{\text{esc},III} = 0.5$ and $\tau_{\text{II}} \approx 0.043$. The increase of τ_0 with $\rho_{\star,III}$ remains quasi-linear

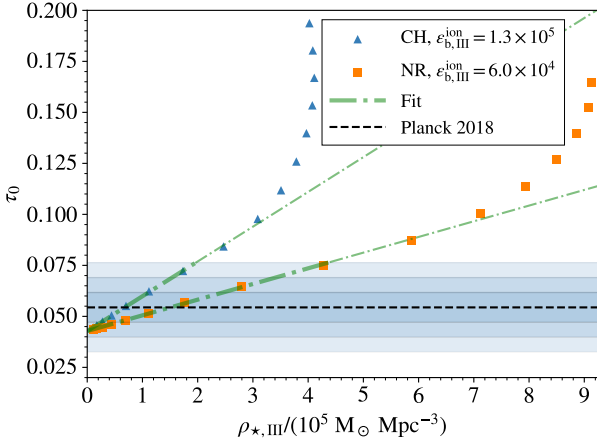


Figure 7. Relation between τ_0 and the CSMD of Pop III stars. The simulation results for the fiducial CH and NR models (with $\alpha = 1$) are shown with the triangles and squares. The thick dash-dotted lines show the general linear fit (Eq. 12) valid for $\tau_0 < 0.0763$ with relative errors $\lesssim 1\%$, whose extrapolation is shown by the thin dash-dotted lines. The Planck measurement of τ_0 (Planck Collaboration 2020) is shown with the dashed line and shaded regions for $1 - 3\sigma$ errors.

for $\tau_0 \lesssim 0.1$ when the IGM is not fully ionized at $z \gtrsim 10$, which covers all NR models with $f_{\star,III} \leq 0.01$. For higher τ_0 , the τ_0 - $\rho_{\star,III}$ relation becomes superlinear driven by (external) ionization feedback, indicating strong self-regulation of Pop III star formation. While increasing $f_{\star,III}$ further beyond 0.01 (up to 0.1), we find an upper limit of $\rho_{\star,III,max} \sim 4$ (9) $\times 10^5 M_{\odot} \text{Mpc}^{-3}$ at $f_{\star,III} \gtrsim 0.03$ (0.1) in the CH (NR) case caused by self-regulation.

These constraints are sensitive to $f_{esc,III}$ and τ_{II} . The former can deviate from our fiducial choice by up to a factor of 2 according to the predictions $f_{esc,III} \sim 0.2 - 0.8$ from Sibony et al. (2022). The latter is determined by the ionization efficiency ζ_{II} and t_{rec} . It is shown in Appendix C that varying t_{rec} only changes τ_{II} by up to a few percent. However, there are larger uncertainties in ζ_{II} (Davies et al. 2021; Davies & Furlanetto 2022; Davies et al. 2024; Mitra & Chatterjee 2023; Asthana et al. 2024) that can modify τ_{II} by a factor of a few. Considering such uncertainties, it is challenging to probe Pop III properties by reionization alone. Stronger constraints can be obtained by combining observations of reionization and the 21-cm signal, as discussed below.

4.3 21-cm signal

To be consistent with the primary interest of current and upcoming radio experiments (e.g., Koopmans et al. 2015; Bowman et al. 2018; Mertens et al. 2021, 2025; de Lera Acedo et al. 2022; Singh et al. 2022; HERA Collaboration 2023; Monsalve et al. 2023; Zhao et al. 2024), we focus on the sky-average global signal $\langle T_{21}(z) \rangle$ and power spectrum Δ^2 of the spatial variations of T_{21} :

$$\langle \tilde{T}_{21}(\mathbf{k}, z) \tilde{T}_{21}^*(\mathbf{k}', z) \rangle = (2\pi)^3 \delta^D(\mathbf{k} - \mathbf{k}') \frac{2\pi^2}{k^3} \Delta^2(k, z), \quad (13)$$

where \mathbf{k} is the comoving wave vector and δ^D is the Dirac delta function. Redshift-space distortions are included in the calculations of $\langle T_{21}(z) \rangle$ and $\Delta^2(k, z)$.

Figure 8 compares the 21-cm predictions from CH (solid) and NR (dotted) models with different values of Pop III SFE $f_{\star,III} \sim 10^{-4} - 0.01$ with fixed $\alpha = 1$ and $t_{rec} = 30$ Myr. The global signal (left panel) is characterized by an absorption ($\langle T_{21} \rangle < 0$) trough

around $z \sim 12 - 30$ followed by a transition to emission and the subsequent decay at $z \lesssim 8$. The rise of absorption (starting from $z \sim 32 - 24$ and reaching the peak at $z \sim 17$) marks the epoch of coupling (EoC), when the spin temperature T_S of neutral hydrogen is driven towards the gas kinetic temperature T_K by the WF effect. Then in the epoch of heating (EoH), $\langle T_{21} \rangle$ increases along with T_K due to the heating of IGM by X-rays, until it becomes positive around $z \sim 11$. Thereafter, $\langle T_{21} \rangle$ converges to zero at lower redshifts as the IGM is increasingly ionized in the EoR. As the Ly α radiation fields become stronger with higher $f_{\star,III}$, facilitating the WF effect during EoC, the absorption trough is deepened and shifted to higher redshifts. The maximum absorption signal varies between $\langle T_{21} \rangle \sim -120$ mK and $\langle T_{21} \rangle \sim -150$ mK, while the timing of peak absorption is relatively stable at $z \sim 16 - 18$, consistent with the timing of the tentative signal detected by EDGES²⁴ (Bowman et al. 2018). Compared with NR stars, the absorption is shallower for CH stars given $\alpha = 1$, and the difference increases with $f_{\star,III}$, reaching ~ 20 mK at $f_{\star,III} = 0.01$. The main reason is that the Lyman-band emission is slightly weaker under CHE (Table 2), because massive ($M_{\star} \gtrsim 50 M_{\odot}$) CH stars are too hot (see Figs. 2 and 3). Considering the constraints from reionization discussed above, we compare the CH and NR models calibrated to the best-fitting value and 3-sigma upper limit of the optical depth for Thomson scattering τ_0 from (Planck Collaboration 2020, see the thick curves in Figs. 6 and 8), finding that the peak absorption is weaker in the CH case by ~ 5 mK (4%) and 15 mK (11%) for $\tau_0 = 0.0544$ (best-fitting) and $\tau_0 = 0.0763$ (3σ upper limit), respectively. The evolution during EoH is mainly regulated by X-rays, which in our case are only produced by Pop II stars, whose formation history has a relatively weak, indirect dependence on $f_{\star,III}$ (see Fig. 4). This explains why the late stage of the transition to emission ($z \lesssim 14$) is almost identical among all cases, except for the CH model with $f_{\star,III} = 0.01$ which shows a faster transition. In this special case already ruled out by the Planck measurement of τ_0 , reionization is significantly accelerated by CHE, such that the volume-averaged ionized fraction of the IGM is already high ($\gtrsim 40\%$) at $z \lesssim 14$ (Fig. 6), reducing the overall strength of the signal (for both absorption and emission). For similar reasons, after the transition, the emission signal decays faster in the CH models and/or for higher $f_{\star,III}$ during EoR.

The 21-cm power spectrum (right panel of Fig. 8) is sensitive to the spatial fluctuations of the Ly α radiation fields, IGM temperature, and ionized/neutral fractions, which dominate the signal during EoC, EoH, and EoR, respectively. Here we focus on the power at a characteristic scale $k = 0.24 \text{ cMpc}^{-1}$ where HERA Collaboration (2023, see their fig. 30) places the strongest observational constraints on the upper limits of Δ^2 . The power spectra as a function of k at fixed redshifts are shown in Appendix D for $k \sim 0.03 - 1 \text{ h cMpc}^{-1}$. At such a relatively large scale, there are three peaks/plateaus in the redshift evolution of 21-cm power spectrum, generally corresponding to the three epochs discussed above. The troughs between them arise from negative cross correlations between the aforementioned fields. The first peak (at $z \sim 19 - 23$) becomes broader with significantly stronger (up to two orders of magnitude) power at $z \gtrsim 24$ (EoC) when $f_{\star,III}$ increases, which accelerates Pop III star formation and enhance the Ly α fields at larger scales during EoC. Nevertheless, the peak power only changes moderately, remaining around $\Delta^2 \sim 50 - 80 \text{ mK}^2$. The

²⁴ Whether this signal has an astrophysical origin is still in debate (e.g., Hills et al. 2018; Bradley et al. 2019; Singh & Subrahmanyan 2019; Singh et al. 2022; Sims & Pober 2020). Therefore, we do not show the EDGES results on our plots.

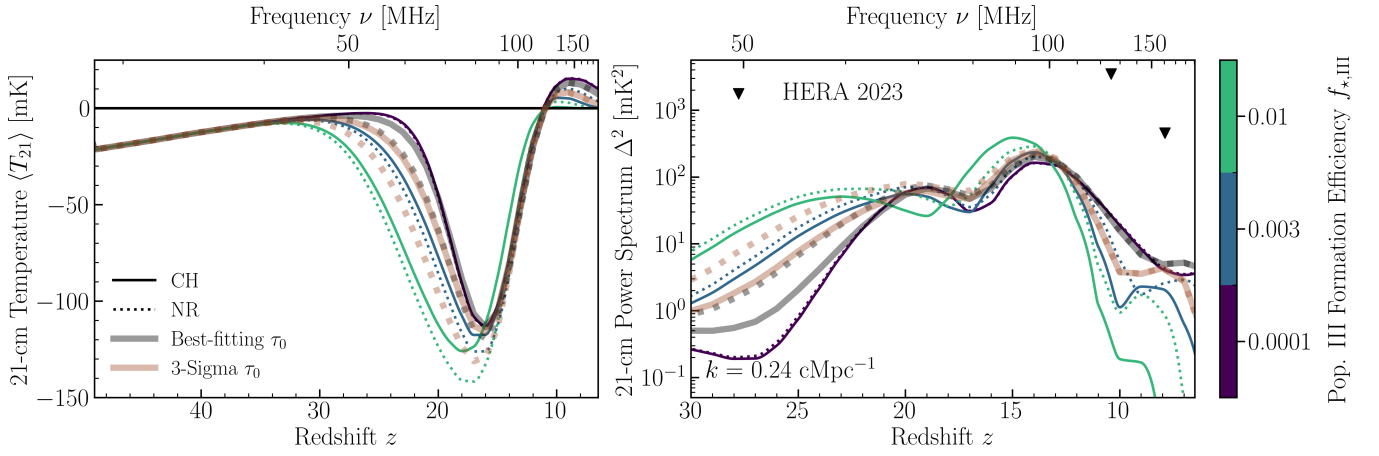


Figure 8. Redshift evolution of the 21-cm global signal (left) and power spectrum (right) with varying $f_{\star, \text{III}} \sim 10^{-4} - 0.01$ (marked on the colorbar) and fixed $\alpha = 1$ and $t_{\text{rec}} = 30$ Myr. As in Fig. 6, the dotted (solid) curves show the results for the NR (CH) Pop III stellar evolution models, and the results for higher $f_{\star, \text{III}}$ are denoted by lighter colours. The gray and brown thick curves show the models with $f_{\star, \text{III}}$ calibrated to the best-fitting value and 3σ upper limit of τ_0 in observations (Planck Collaboration 2020), respectively. In the right panel, we show the power at a characteristic scale $k = 0.24 \text{ cMpc}^{-1}$, compared with the observational constraints (2σ upper limits) from HERA Collaboration (2023), which are denoted as triangles.

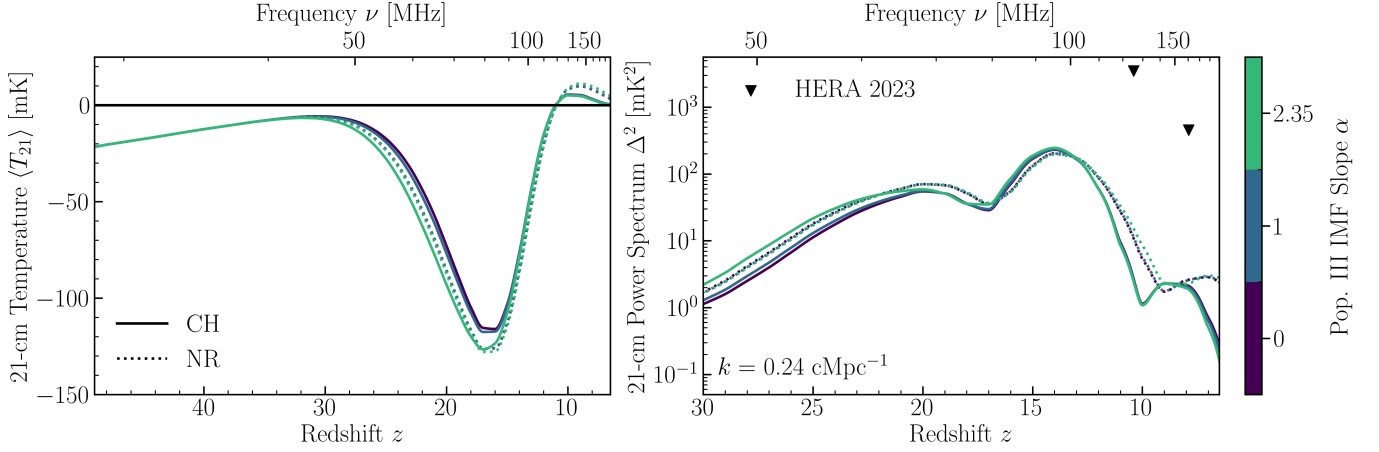


Figure 9. The 21-cm signal. Same as Fig. 8 but varying the Pop III IMF slope α (0, 1, and 2.35) with fixed SFE $f_{\star, \text{III}} = 0.003$ and recovery time $t_{\text{rec}} = 30$ Myr.

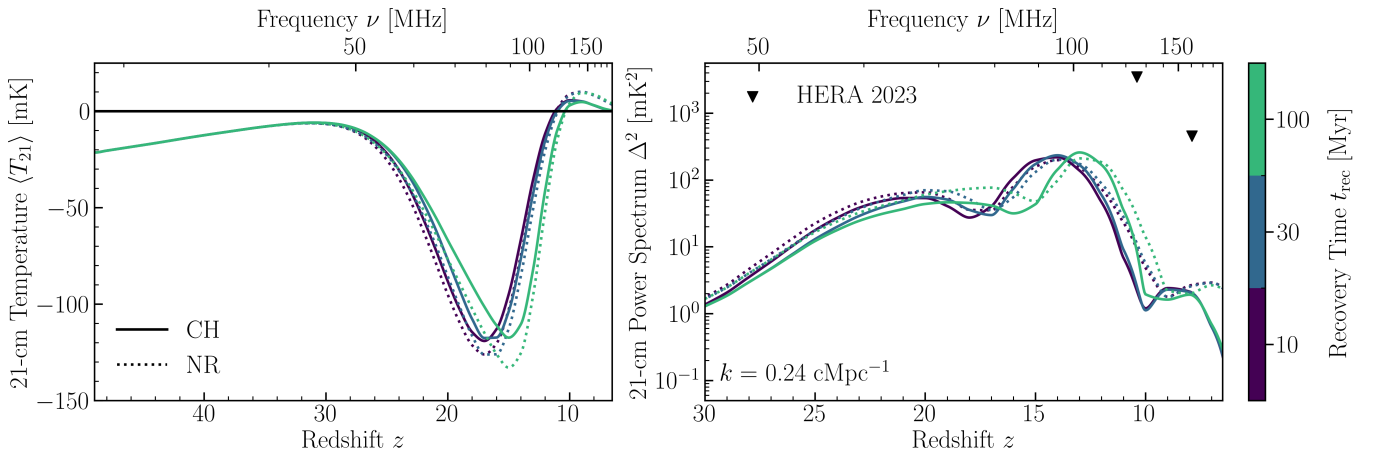


Figure 10. The 21-cm signal. Same as Fig. 8 but varying the recovery time t_{rec} (10, 30, and 100 Myr) with fixed Pop III SFE $f_{\star, \text{III}} = 0.003$ and IMF slope $\alpha = 1$.

peak power is slightly weaker in the CH models compared with the NR case, as expected from the reduction of Lyman-band emission by CHE. When τ_0 is controlled (thick curves), the power from CH stars is lower than that from NR stars by a factor of $\sim 2 - 3$ during EoC ($z \sim 24 - 30$) due to weaker Ly α coupling with reduced $f_{\star, \text{III}}$. The second (strongest) peak around $z \sim 14$ with $\Delta^2 \sim 200 \text{ mK}^2$ shows very small variations for the models that are consistent with the observational constraints from reionization (i.e., $f_{\star, \text{III}} \lesssim 0.002$ and $f_{\star, \text{III}} \lesssim 0.004$ for CH and NR stars, respectively), similar to the behavior of the global signal during EoH. Again, the reason is that EoH is dominated by X-ray heating from Pop II stars and these models have almost identical Pop II star formation histories (Fig. 4). However, for models with larger $f_{\star, \text{III}}$ and accelerated IGM ionization, like in the extreme case of $f_{\star, \text{III}} = 0.01$, the peak is enhanced and shifted to higher redshifts, reaching up to $\Delta^2 \sim 500 \text{ mK}^2$ at $z = 15$ for CH stars. This is caused by the suppression of Pop II star formation in ionized regions, i.e., external ionization feedback, which reduces X-ray heating around ionized bubbles, leading to less negative contributions from the cross power between X-ray heating and neutral hydrogen density. Finally, when IGM ionization is facilitated either by CHE or increasing $f_{\star, \text{III}}$, the power during EoR ($z \lesssim 12$) decreases dramatically, and the third peak/plateau (at $z \lesssim 9$) is narrower and shifted to higher redshifts, which covers a broad range $\Delta^2 \sim 0.2 - 7 \text{ mK}^2$.

Next, we explore the effects of α and t_{rec} while fixing Pop III SFE to the fiducial value $f_{\star, \text{III}} = 0.003$, as shown in Figs. 9 (for $\alpha \sim 0 - 2.35$ and $t_{\text{rec}} = 30 \text{ Myr}$) and 10 (for $t_{\text{rec}} \sim 10 - 100 \text{ Myr}$ and $\alpha = 1$), respectively. The effects are generally smaller with α compared to those of $f_{\star, \text{III}}$, especially for NR stars. This is reasonable because the lower mass bound of our IMFs is fixed to a relatively high value ($9 M_{\odot}$), above which the production efficiency $\epsilon_b(M_{\star})$ of UV photons is not very sensitive to stellar mass (Fig. 3). Besides, it is shown in Gessey-Jones et al. (2022) that the 21-cm signal varies modestly across a broader range of IMFs for NR Pop III stars if one only considers the impact of IMF on Lyman band radiation. The variation can be significantly boosted when the impact of Pop III IMF on XRBs is considered (Sartorio et al. 2023; Gessey-Jones et al. 2025), which we leave to future work. CHE weakens the global absorption signal and generally reduces the power during EoC ($z \gtrsim 17$) for $\alpha \lesssim 1$, while the opposite happens for $\alpha = 2.35$. In the former (latter) case, the IMF-averaged Lyman-band emission from CH stars is reduced (enhanced) compared with NR stars, as shown Table 2. Due to this trend reversal, the CH models show a much stronger dependence on α , where the peak global absorption signal varies by $\sim 10 \text{ mK}$ for $\alpha \sim 0 - 2.35$. Yet in the CH model with $\alpha = 2.35$, the global absorption signal is still weaker compared with the NR case at $z \lesssim 17$, and the power is lower at $z \sim 21 - 17$, which can be attributed to accelerated IGM ionization by CHE. During EoH and EoR ($z \lesssim 16$), both CH and NR models are not sensitive to α , and their differences are consistent with the trends discussed above for $f_{\star, \text{III}} = 0.01$ and $\alpha = 1$. A noticeable feature is that the power during EoR ($z \lesssim 11$) is slightly higher for $\alpha = 2.35$ compared with $\alpha \lesssim 1$ in the NR case, but lower in the CH case. This arises from the different relations between ϵ_b^{ion} and α in the two stellar evolution models, which reflects the difference in the stellar mass dependence of production efficiency of ionizing photons (Fig. 3).

Fig. 10 shows that t_{rec} mainly affects the timings of the three epochs, as it regulates the formation history of Pop II stars (Magg et al. 2022a). For both CH and NR stars, the peak global absorption signal is shifted from $z \sim 17$ to $z \sim 15$ when t_{rec} is increased from 10 Myr to 100 Myr, delaying the transition from EoC to EoH. Similar shifts occur in the evolution of $\Delta^2 (k = 0.24 \text{ cMpc}^{-1})$. The lowest

point of global signal remains around $\langle T_{21} \rangle \sim -120 \text{ mK}$ for CH stars, while it drops from $\langle T_{21} \rangle \sim -130 \text{ mK}$ with $t_{\text{rec}} \lesssim 30 \text{ Myr}$ to $\langle T_{21} \rangle \sim -135 \text{ mK}$ with $t_{\text{rec}} = 100 \text{ Myr}$ in the NR models due to the delay of X-ray heating. This deepening does not occur in the CH case because the delay of heating is counter balanced by the acceleration of IGM ionization.

In general, the effects of CHE on the 21-cm signal are weaker than those of varying $f_{\star, \text{III}}$ but comparable to the effects of α and t_{rec} for $f_{\star, \text{III}} \lesssim 0.003$. Stronger effects of CHE can be achieved through IGM ionization given higher $f_{\star, \text{III}}$, but such cases are already ruled out by the Planck Collaboration (2020) measurement of τ_0 (see Sec. 4.2). However, it is shown in Fig. 8 that when different values of $f_{\star, \text{III}}$ are chosen to reproduce the same value of τ_0 within the constraints from Planck Collaboration (2020) for CH and NR Pop III stars, the two cases show significant differences in the 21-cm signal. On the other hand, α and t_{rec} do not show this feature because they have much weaker effects on the IGM ionization history (Appendix C). This implies that it is promising to jointly constrain $f_{\star, \text{III}}$ and the fraction of CH stars in Pop III by combining observations of the 21-cm signal and ionization history, although existing observations are not sensitive enough to provide meaningful results. The power spectra predicted by our simulations remains below the upper limits placed by HERA Collaboration (2023) by at least 2 orders of magnitude. We defer a detailed evaluation of the feasibility of such joint constraints considering the improved sensitivities of upcoming observations to future work (for an example of such analysis see Muñoz et al. 2022).

5 SUMMARY AND DISCUSSION

We use detailed stellar atmosphere models (Sec. 2) to investigate how chemically homogeneous evolution (CHE), driven by rapid rotation, affects the UV spectra of metal-free Population III (Pop III) stars. These spectra are incorporated in state-of-the-art semi-numerical simulations (Sec. 3) to explore the impact of Pop III CHE on early star/galaxy formation and evolution of the intergalactic medium (IGM) probed by the 21-cm signal and reionization history. Different assumptions are considered for the formation efficiency (SFE) and initial mass function (IMF) of Pop III stars, as well as the transition from Pop III to metal-enriched Population II (Pop II) star formation.

Our results demonstrate that CHE significantly boosts the emission efficiency $\epsilon_{\text{b,III}}^{\text{ion}}$ of ionizing photons from Pop III stars (by a factor of $\sim 2 - 6$ in the stellar mass range $M_{\star} \in [9, 300] M_{\odot}$), leading to stronger constraints on Pop III star formation from observations of reionization. In particular, we derive a general relation between the Thomson scattering optical depth τ_0 with $\epsilon_{\text{b,III}}^{\text{ion}}$, the average escape fraction of ionizing photons $f_{\text{esc,III}}$, and the stellar mass density $\rho_{\star, \text{III}}$ of Pop III stars ever formed (see also Visbal et al. 2015; Inayoshi et al. 2016). We find that the $\rho_{\star, \text{III}}$ allowed/required to explain the measurement of τ_0 by Planck Collaboration (2020) is reduced by a factor of ~ 2 under CHE, given a log-flat top-heavy IMF expected from small-scale simulations of primordial star formation. Meanwhile, the emission efficiency $\epsilon_{\text{b,III}}^{\text{Ly}}$ of Lyman-band photons (10.2 – 13.6 eV) is slightly reduced by CHE. The lower $\rho_{\star, \text{III}}$ and $\epsilon_{\text{b,III}}^{\text{Ly}}$ lead to shallower 21-cm global absorption signals, with reductions of up to $\sim 15 \text{ mK}$ (11%) in peak absorption at $z \sim 17$, and the suppression of large-scale ($k \sim 0.2 \text{ cMpc}^{-1}$) power at high redshifts ($z \gtrsim 25$) by a factor of a few. These effects are modulated by variations in Pop III star formation parameters, which generally have comparable effects on the 21-cm signal and reionization as CHE, highlighting the interplay

between stellar evolution (e.g., rotation and mixing leading to CHE) and star/galaxy formation (e.g., SFE, IMF, and transition from Pop III to Pop II star formation) in early cosmic evolution.

Focusing on the UV emission from Pop III stars during main sequence (MS), our work is a step towards the challenging yet promising goal of jointly constraining stellar evolution and star/galaxy formation during Cosmic Dawn from observations of the 21-cm signal and reionization. The main caveat is our ignorance of X-ray binaries (XRBs) from Pop III stars, which could completely change the picture (Gessey-Jones et al. 2025) considering the potentially strong dependence of their X-ray outputs on the IMF and binary statistics (e.g., Fragos et al. 2013a; Ryu et al. 2016; Liu et al. 2021a; Sartorio et al. 2023; Liu et al. 2024a). Previous studies have shown that CHE has strong effects on binary stellar evolution (de Mink & Mandel 2016; Mandel & de Mink 2016; Marchant et al. 2017, 2023; du Buisson et al. 2020; Riley et al. 2021; Qin et al. 2023; Dall’Amico et al. 2025; Vigna-Gómez et al. 2025). However, they mostly focus on compact object mergers and suffer from large uncertainties in binary population synthesis models, especially in the metal-poor regime with sparse observational constraints and discrepant simulation results²⁵, such that the impact of CHE on high- z XRBs is poorly understood. Another limitation is that our simulations only explore a limited part of the vast parameter space of semi-numerical simulations of Cosmic Dawn, focusing on Pop III star formation. The other processes, such as escape of ionizing photons into the IGM, Pop II star formation and X-ray heating, are modelled by constant parameters with values chosen from low-redshift observations or calibrated to reproduce the observed cosmic star formation rate density at $z \sim 6 - 8$. Improving the theoretical models and their calibrations in these aspects is an ongoing effort of the community (e.g., Muñoz et al. 2022; Feathers et al. 2024; Dhandha et al. 2025, Dasgupta et al. in prep.), which is crucial for better understanding the role of CHE in follow-up studies.

Moreover, the broader implications of CHE extend beyond the 21-cm signal and reionization. As discussed in Liu et al. (2025), CHE can significantly enhance the rest-frame UV luminosities of high- z star-forming galaxies, potentially explaining the overabundance of UV-bright galaxies observed by the JWST at $z \gtrsim 10$ (e.g., Donnan et al. 2023, 2024; Finkelstein et al. 2023, 2024; Harikane et al. 2023; Adams et al. 2024) without invoking drastic changes to the ‘standard’ model of galaxy formation. Moreover, CHE also regulates the post-MS and binary stellar evolution of massive stars, affecting the properties of Wolf-Rayet stars, supernovae, gamma-ray bursts, X-ray binaries, and binary compact object mergers (e.g., Eldridge & Stanway 2012; Yoon et al. 2012; Szécsi et al. 2015; Mandel & de Mink 2016; de Mink & Mandel 2016; Marchant et al. 2017; Kubátová et al. 2019; du Buisson et al. 2020; Riley et al. 2021; Qin et al. 2023; Umeda & Nagele 2024; Dall’Amico et al. 2025; Vigna-Gómez et al. 2025). Finally, CHE and fast rotation in general have profound implications for the chemical enrichment of the early Universe with their unique nucleosynthetic signatures (e.g., Chiappini et al. 2006, 2011; Chiappini 2013; Maeder et al. 2015; Choplin et al. 2017, 2019; Liu et al. 2021b; Jeena et al. 2023; Tsiatsiou et al. 2024; Nandal et al. 2024), which can explain the peculiar chemical abundance patterns of high- z galaxies (Bunker et al. 2023; D’Eugenio et al. 2023; Cameron et al. 2023; Senchyna et al. 2023; Ji et al. 2024; Schaerer et al. 2024;

Topping et al. 2024) and extremely metal-poor stars in the local Universe (e.g., Yoon et al. 2016, 2018; Hansen et al. 2019; Dietz et al. 2021; Zepeda et al. 2023).

In conclusion, our findings underscore the importance of considering CHE and stellar rotation in general in models of early star formation and galaxy evolution. The enhanced UV and ionizing radiation from CHE stars as well as nucleosynthesis regulated by rotation and mixing not only impact the 21-cm signal and reionization but may also provide viable explanations for the observed properties of high- z galaxies, energetic transients, and nearby extremely metal-poor stars. Future studies should further systematically and self-consistently explore the effects of CHE on various physical processes and observables to pave the way for joint observational constraints on the physics of stellar evolution and star/galaxy formation.

ACKNOWLEDGMENTS

The authors thank Furen Deng for useful discussions on 21cmSPACE. BL gratefully acknowledges the funding of the Royal Society University Research Fellowship and the Deutsche Forschungsgemeinschaft (DFG, German Research Foundation) under Germany’s Excellence Strategy EXC 2181/1 - 390900948 (the Heidelberg STRUCTURES Excellence Cluster). TGJ acknowledges the support of the Science and Technology Facilities Council (STFC) through the grant number ST/V506606/1. JD acknowledges support from the Boustany Foundation and Cambridge Commonwealth Trust in the form of an Isaac Newton Studentship. YS and GM have received funding from the European Research Council (ERC) under the European Union’s Horizon 2020 research and innovation programme (grant agreement No. 833925, project STAREX).

DATA AVAILABILITY

The full spectra $L_\nu(t)$, production rates of UV photons in 5 bands, and underlying stellar properties of CH Pop III stars during MS are available at [10.5281/zenodo.15111273](https://doi.org/10.5281/zenodo.15111273), alongside with the MS lifetime-average production rates of UV photons $M_\star \epsilon_b / t_{\text{MS}}$ in 7 bands for the NR Pop III stars modelled by Gessey-Jones et al. (2022). For the latter (NR Pop III stars), the Lyman-band lifetime-integrated spectra $\epsilon(\nu; M_\star)$ are available at [10.5281/zenodo.5553052](https://doi.org/10.5281/zenodo.5553052).

REFERENCES

- Abe M., Yajima H., Khochfar S., Dalla Vecchia C., Omukai K., 2021, *MNRAS*, **508**, 3226
- Adams N. J., et al., 2024, *ApJ*, **965**, 169
- Algera H. S. B., et al., 2023, *MNRAS*, **518**, 6142
- Angel R., et al., 2008, *ApJ*, **680**, 1582
- Aryan A., Pandey S. B., Gupta R., Ror A. K., 2023, *MNRAS*, **521**, L17
- Asthana S., Kulkarni G., Haehnelt M. G., Bolton J. S., Keating L. C., Simmonds C., 2024, *arXiv e-prints*, p. [arXiv:2412.01906](https://arxiv.org/abs/2412.01906)
- Barkana R., 2016, *Phys. Rep.*, **645**, 1
- Barkana R., Loeb A., 2004, *ApJ*, **609**, 474
- Barkana R., Loeb A., 2005, *ApJ*, **626**, 1
- Barkana R., Loeb A., 2011, *MNRAS*, **415**, 3113
- Behroozi P., Wechsler R. H., Hearin A. P., Conroy C., 2019, *MNRAS*, **488**, 3143
- Benitez-Llambay A., Frenk C., 2020, *MNRAS*, **498**, 4887
- Bevins H. T. J., Heimersheim S., Abril-Cabezas I., Fialkov A., de Lera Acedo E., Handley W., Singh S., Barkana R., 2023, *arXiv e-prints*, p. [arXiv:2301.03298](https://arxiv.org/abs/2301.03298)

²⁵ Our simple assumption of no Pop III XRBs is motivated by the rareness of close binaries of Pop III stars in recent simulations of Pop III star clusters (e.g., Sugimura et al. 2020, 2023; Liu et al. 2021a; Park et al. 2023, 2024). However, previous simulations with different configurations of Pop III clusters have produced large fractions of close binaries (e.g., Ryu et al. 2016).

- Bowman J. D., Rogers A. E. E., Monsalve R. A., Mozdzen T. J., Mahesh N., 2018, *Nature*, **555**, 67
- Bradley R. F., Tauscher K., Rapetti D., Burns J. O., 2019, *ApJ*, **874**, L53
- Bromm V., 2013, *Reports on Progress in Physics*, **76**, 112901
- Bromm V., Kudritzki R. P., Loeb A., 2001, *ApJ*, **552**, 464
- Bromm V., Yoshida N., Hernquist L., McKee C. F., 2009, *Nature*, **459**, 49
- Brott I., et al., 2011, *A&A*, **530**, A115
- Bunker A. J., et al., 2023, *A&A*, **677**, A88
- Cameron A. J., Katz H., Rey M. P., Saxena A., 2023, *MNRAS*, **523**, 3516
- Cen R., 2003, *ApJ*, **591**, L2
- Chatterjee A., Dayal P., Choudhury T. R., Schneider R., 2020, *MNRAS*, **496**, 1445
- Chen K.-J., Tang C.-Y., Whalen D. J., Ho M.-Y., Tsai S.-H., Ou P.-S., Ono M., 2024, *ApJ*, **964**, 91
- Chiaki G., Wise J. H., 2019, *MNRAS*, **482**, 3933
- Chiaki G., Susa H., Hirano S., 2018, *MNRAS*, **475**, 4378
- Chiappini C., 2013, *Astronomische Nachrichten*, **334**, 595
- Chiappini C., Hirschi R., Meynet G., Ekström S., Maeder A., Matteucci F., 2006, *A&A*, **449**, L27
- Chiappini C., Frischknecht U., Meynet G., Hirschi R., Barbuy B., Pignatari M., Decressin T., Maeder A., 2011, *Nature*, **472**, 454
- Chon S., Omukai K., Schneider R., 2021, *MNRAS*, **508**, 4175
- Choplin A., Hirschi R., Meynet G., Ekström S., 2017, *A&A*, **607**, L3
- Choplin A., Tominaga N., Ishigaki M. N., 2019, *A&A*, **632**, A62
- Cohen A., Fialkov A., Barkana R., 2016, *MNRAS*, **459**, L90
- Cohen A., Fialkov A., Barkana R., Lotem M., 2017, *MNRAS*, **472**, 1915
- Cohen A., Fialkov A., Barkana R., 2018, *MNRAS*, **478**, 2193
- Costa G., et al., 2025, *A&A*, **694**, A193
- D'Eugenio F., et al., 2023, *arXiv e-prints*, p. arXiv:2311.09908
- Dall'Amico M., Mapelli M., Iorio G., Costa G., Charlot S., Korb E., Sgalletta C., Lecroq M., 2025, *arXiv e-prints*, p. arXiv:2501.04778
- Davies F. B., Furlanetto S. R., 2022, *MNRAS*, **514**, 1302
- Davies F. B., Bosman S. E. I., Furlanetto S. R., Becker G. D., D'Aloisio A., 2021, *ApJ*, **918**, L35
- Davies F. B., Bosman S. E. I., Furlanetto S. R., 2024, *arXiv e-prints*, p. arXiv:2406.18186
- Dayal P., Ferrara A., 2018, *Phys. Rep.*, **780**, 1
- Dayal P., et al., 2020, *MNRAS*, **495**, 3065
- Dhandha J., et al., 2025, *arXiv e-prints*, p. arXiv:2503.21687
- Dietz S. E., Yoon J., Beers T. C., Placco V. M., Lee Y. S., 2021, *ApJ*, **914**, 100
- Donnan C. T., et al., 2023, *MNRAS*, **518**, 6011
- Donnan C. T., et al., 2024, *MNRAS*, **533**, 3222
- Eide M. B., Graziani L., Ciardi B., Feng Y., Kakiichi K., Di Matteo T., 2018, *MNRAS*, **476**, 1174
- Ekström S., Meynet G., Chiappini C., Hirschi R., Maeder A., 2008, *A&A*, **489**, 685
- Eldridge J. J., Stanway E. R., 2012, *MNRAS*, **419**, 479
- Ewall-Wice A., Chang T. C., Lazio J., Doré O., Seiffert M., Monsalve R. A., 2018, *ApJ*, **868**, 63
- Feathers C., Kulkarni M., Visbal E., 2024, *arXiv e-prints*, p. arXiv:2411.07875
- Feng C., Holder G., 2018, *ApJ*, **858**, L17
- Fialkov A., Barkana R., 2014, *MNRAS*, **445**, 213
- Fialkov A., Barkana R., 2019, *MNRAS*, **486**, 1763
- Fialkov A., Barkana R., Tseliakhovich D., Hirata C. M., 2012, *MNRAS*, **424**, 1335
- Fialkov A., Barkana R., Visbal E., Tseliakhovich D., Hirata C. M., 2013, *MNRAS*, **432**, 2909
- Fialkov A., Barkana R., Pinhas A., Visbal E., 2014a, *MNRAS*, **437**, L36
- Fialkov A., Barkana R., Visbal E., 2014b, *Nature*, **506**, 197
- Fialkov A., Cohen A., Barkana R., Silk J., 2017, *MNRAS*, **464**, 3498
- Fialkov A., Gessey-Jones T., Dhandha J., 2023, *arXiv e-prints*, p. arXiv:2311.05366
- Field G. B., 1958, *Proceedings of the IRE*, **46**, 240
- Field G. B., 1959, *ApJ*, **129**, 551
- Finkelstein S. L., 2016, *Publ. Astron. Soc. Australia*, **33**, e037
- Finkelstein S. L., et al., 2023, *ApJ*, **946**, L13
- Finkelstein S. L., et al., 2024, *ApJ*, **969**, L2
- Fragos T., et al., 2013a, *ApJ*, **764**, 41
- Fragos T., Lehmer B. D., Naoz S., Zezas A., Basu-Zych A., 2013b, *ApJ*, **776**, L31
- Frebel A., Norris J. E., 2015, *ARA&A*, **53**, 631
- Fujimoto S., et al., 2025, *arXiv e-prints*, p. arXiv:2501.11678
- Furlanetto S. R., Oh S. P., 2005, *MNRAS*, **363**, 1031
- Furlanetto S. R., Zaldarriaga M., Hernquist L., 2004, *ApJ*, **613**, 1
- Garaldi E., 2023, *The Journal of Open Source Software*, **8**, 5407
- Gardner J. P., et al., 2006, *Space Sci. Rev.*, **123**, 485
- Gessey-Jones T., et al., 2022, *MNRAS*, **516**, 841
- Gessey-Jones T., Fialkov A., de Lera Acedo E., Handley W. J., Barkana R., 2023, *MNRAS*, **526**, 4262
- Gessey-Jones T., et al., 2025, *arXiv e-prints*, p. arXiv:2502.18098
- Ghodla S., Eldridge J. J., Stanway E. R., Stevance H. F., 2022, *MNRAS*, **518**, 860
- Götberg Y., de Mink S. E., McQuinn M., Zapartas E., Groh J. H., Norman C., 2020, *A&A*, **634**, A134
- Greif T. H., Springel V., White S. D. M., Glover S. C. O., Clark P. C., Smith R. J., Klessen R. S., Bromm V., 2011, *ApJ*, **737**, 75
- Greif T. H., Bromm V., Clark P. C., Glover S. C. O., Smith R. J., Klessen R. S., Yoshida N., Springel V., 2012, *MNRAS*, **424**, 399
- Grisdale K., Thatte N., Devriendt J., Pereira-Santaella M., Slyz A., Kimm T., Dubois Y., Yi S. K., 2021, *MNRAS*, **501**, 5517
- HERA Collaboration 2022, *ApJ*, **925**, 221
- HERA Collaboration 2023, *ApJ*, **945**, 124
- Haemmerlé L., Mayer L., Klessen R. S., Hosokawa T., Madau P., Bromm V., 2020, *Space Sci. Rev.*, **216**, 48
- Hansen C. J., Hansen T. T., Koch A., Beers T. C., Nordström B., Placco V. M., Andersen J., 2019, *A&A*, **623**, A128
- Harikane Y., et al., 2023, *ApJS*, **265**, 5
- Hartwig T., Bromm V., Klessen R. S., Glover S. C. O., 2015, *MNRAS*, **447**, 3892
- Hartwig T., et al., 2022, *ApJ*, **936**, 45
- Hartwig T., Lipatova V., Glover S. C. O., Klessen R. S., 2024, *MNRAS*, **535**, 516
- Hassan S., et al., 2023, *arXiv e-prints*, p. arXiv:2305.02703
- Heger A., Woosley S. E., 2010, *ApJ*, **724**, 341
- Hills R., Kulkarni G., Meerburg P. D., Puchwein E., 2018, *Nature*, **564**, E32
- Hirano S., Bromm V., 2017, *MNRAS*, **470**, 898
- Hirano S., Bromm V., 2018, *MNRAS*, **476**, 3964
- Hirano S., Machida M. N., 2022, *ApJ*, **935**, L16
- Hirano S., Hosokawa T., Yoshida N., Umeda H., Omukai K., Chiaki G., Yorke H. W., 2014, *ApJ*, **781**, 60
- Hirano S., Hosokawa T., Yoshida N., Omukai K., Yorke H. W., 2015, *MNRAS*, **448**, 568
- Hirano S., Yoshida N., Sakurai Y., Fujii M. S., 2018, *ApJ*, **855**, 17
- Hirano S., Machida M. N., Basu S., 2021, *ApJ*, **917**, 34
- Hirano S., Shen Y., Nishijima S., Sakai Y., Umeda H., 2023, *MNRAS*, **525**, 5737
- Hubeny I., 1988, *Computer Physics Communications*, **52**, 103
- Hubeny I., Lanz T., 2017a, *arXiv e-prints*, p. arXiv:1706.01859
- Hubeny I., Lanz T., 2017b, *arXiv e-prints*, p. arXiv:1706.01935
- Hubeny I., Lanz T., 2017c, *arXiv e-prints*, p. arXiv:1706.01937
- Hubeny I., Allende Prieto C., Osorio Y., Lanz T., 2021, *arXiv e-prints*, p. arXiv:2104.02829
- Inayoshi K., Kashiyama K., Visbal E., Haiman Z., 2016, *MNRAS*, **461**, 2722
- Ishigaki M. N., Tominaga N., Kobayashi C., Nomoto K., 2018, *ApJ*, **857**, 46
- Jaacks J., Thompson R., Finkelstein S. L., Bromm V., 2018, *MNRAS*, **475**, 4396
- Jaacks J., Finkelstein S. L., Bromm V., 2019, *MNRAS*, **488**, 2202
- Jeena S. K., Banerjee P., Chiaki G., Heger A., 2023, *MNRAS*, **526**, 4467
- Jeon M., Pawlik A. H., Bromm V., Milosavljević M., 2014, *MNRAS*, **444**, 3288
- Ji A. P., Frebel A., Bromm V., 2015, *MNRAS*, **454**, 659
- Ji X., et al., 2024, *arXiv e-prints*, p. arXiv:2404.04148
- Johnson J. L., Dalla Vecchia C., Khochfar S., 2013, *MNRAS*, **428**, 1857

- Kamran M., Ghara R., Majumdar S., Mellema G., Bharadwaj S., Pritchard J. R., Mondal R., Iliiev I. T., 2022, arXiv e-prints, p. arXiv:2207.09128
- Karlsson T., Bromm V., Bland-Hawthorn J., 2013, *Reviews of Modern Physics*, **85**, 809
- Katz H., Kimm T., Ellis R. S., Devriendt J., Slyz A., 2022, arXiv e-prints, p. arXiv:2207.04751
- Katz H., Kimm T., Ellis R. S., Devriendt J., Slyz A., 2023, *MNRAS*, **524**, 351
- Kaur H. D., Qin Y., Mesinger A., Pallottini A., Fragos T., Basu-Zych A., 2022, *MNRAS*, **513**, 5097
- Kim S. Y., et al., 2024, arXiv e-prints, p. arXiv:2408.15214
- Kimura K., Hosokawa T., Sugimura K., Fukushima H., 2023, *ApJ*, **950**, 184
- Klessen R. S., Glover S. C. O., 2023, *ARA&A*, **61**, 65
- Koopmans L., et al., 2015, in *Advancing Astrophysics with the Square Kilometre Array (AASKA14)*. p. 1 (arXiv:1505.07568), doi:10.22323/1.215.0001
- Koutsouridou I., Salvadori S., Skúladóttir Á., 2023, arXiv e-prints, p. arXiv:2312.05309
- Kroupa P., 2001, *MNRAS*, **322**, 231
- Kubátová B., et al., 2019, *A&A*, **623**, A8
- Lanz T., Hubeny I., 2003, *ApJS*, **146**, 417
- Lanz T., Hubeny I., 2007, *ApJS*, **169**, 83
- Larkin M. M., Gerasimov R., Burgasser A. J., 2023, *AJ*, **165**, 2
- Latif M. A., Schleicher D., 2020, *ApJ*, **902**, L31
- Latif M. A., Whalen D., Khochfar S., 2022, *ApJ*, **925**, 28
- Lecroq M., et al., 2025, arXiv e-prints, p. arXiv:2502.14028
- Lehmer B. D., Eufrazio R. T., Basu-Zych A., Garofali K., Gilbertson W., Mesinger A., Yukita M., 2022, *ApJ*, **930**, 135
- Lewis A., Bridle S., 2002, *Phys. Rev. D*, **66**, 103511
- Lewis A., Challinor A., 2011, *CAMB: Code for Anisotropies in the Microwave Background*, Astrophysics Source Code Library, record ascl:1102.026
- Lewis A., Challinor A., Lasenby A., 2000, *ApJ*, **538**, 473
- Lewis J. S. W., et al., 2022, *MNRAS*, **516**, 3389
- Liu B., Bromm V., 2020a, *MNRAS*, **495**, 2475
- Liu B., Bromm V., 2020b, *MNRAS*, **497**, 2839
- Liu B., Meynet G., Bromm V., 2021a, *MNRAS*, **501**, 643
- Liu B., Sibony Y., Meynet G., Bromm V., 2021b, *MNRAS*, **506**, 5247
- Liu B., Sartorio N. S., Izzard R. G., Fialkov A., 2024a, *MNRAS*, **527**, 5023
- Liu B., Gurian J., Inayoshi K., Hirano S., Hosokawa T., Bromm V., Yoshida N., 2024b, *MNRAS*, **534**, 290
- Liu B., Sibony Y., Meynet G., Bromm V., 2025, *ApJ*, **980**, L30
- Madau P., Dickinson M., 2014, *ARA&A*, **52**, 415
- Madau P., Fragos T., 2017, *ApJ*, **840**, 39
- Madau P., Meiksin A., Rees M. J., 1997, *ApJ*, **475**, 429
- Maeder A., Meynet G., 2000, *ARA&A*, **38**, 143
- Maeder A., Meynet G., Chiappini C., 2015, *A&A*, **576**, A56
- Magg M., et al., 2022a, *MNRAS*, **514**, 4433
- Magg M., Schauer A. T. P., Klessen R. S., Glover S. C. O., Tress R. G., Jaura O., 2022b, *ApJ*, **929**, 119
- Maiolino R., et al., 2024, *A&A*, **687**, A67
- Mandel I., de Mink S. E., 2016, *MNRAS*, **458**, 2634
- Marchant P., Langer N., Podsiadlowski P., Tauris T. M., de Mink S., Mandel I., Moriya T. J., 2017, *A&A*, **604**, A55
- Marchant P., Podsiadlowski P., Mandel I., 2023, arXiv e-prints, p. arXiv:2311.14041
- Martinet S., Meynet G., Ekström S., Georgy C., Hirschi R., 2023, arXiv e-prints, p. arXiv:2309.00062
- Martins F., Hillier D. J., Boutet J. C., Depagne E., Foellmi C., Marchenko S., Moffat A. F., 2009, *A&A*, **495**, 257
- Martins F., Depagne E., Russeil D., Mahy L., 2013, *A&A*, **554**, A23
- McKee C. F., Stacy A., Li P. S., 2020, *MNRAS*, **496**, 5528
- Mebane R. H., Mirocha J., Furlanetto S. R., 2018, *MNRAS*, **479**, 4544
- Mertens F. G., Semelin B., Koopmans L. V. E., 2021, in Siebert A., et al., eds, *SF2A-2021: Proceedings of the Annual meeting of the French Society of Astronomy and Astrophysics*. pp 211–214 (arXiv:2109.10055), doi:10.48550/arXiv.2109.10055
- Mertens F. G., et al., 2025, arXiv e-prints, p. arXiv:2503.05576
- Mesinger A., Furlanetto S., Cen R., 2011, *MNRAS*, **411**, 955
- Meynet G., Ekström S., Maeder A., 2006, *A&A*, **447**, 623
- Mirocha J., Furlanetto S. R., 2019, *MNRAS*, **483**, 1980
- Mitra S., Chatterjee A., 2023, *MNRAS*, **523**, L35
- Mo H., van den Bosch F. C., White S., 2010, *Galaxy Formation and Evolution*. Cambridge Univ. Press, Cambridge
- Mondal R., Barkana R., 2023, arXiv e-prints, p. arXiv:2305.08593
- Monsalve R. A., et al., 2023, arXiv e-prints, p. arXiv:2309.02996
- Muñoz J. B., Qin Y., Mesinger A., Murray S. G., Greig B., Mason C., 2022, *MNRAS*, **511**, 3657
- Murphy L. J., et al., 2021, *MNRAS*, **501**, 2745
- Nakajima K., Maiolino R., 2022, *MNRAS*, **513**, 5134
- Nandal D., Farrell E., Buldgen G., Meynet G., Ekstrom S., 2023, arXiv e-prints, p. arXiv:2309.04435
- Nandal D., Sibony Y., Tsiatsiou S., 2024, *A&A*, **688**, A142
- Naoz S., Yoshida N., Barkana R., 2011, *MNRAS*, **416**, 232
- Naoz S., Yoshida N., Gnedin N. Y., 2013, *ApJ*, **763**, 27
- Pacucci F., Mesinger A., Mineo S., Ferrara A., 2014, *MNRAS*, **443**, 678
- Park J., Mesinger A., Greig B., Gillet N., 2019, *MNRAS*, **484**, 933
- Park J., Ricotti M., Sugimura K., 2023, *MNRAS*, **521**, 5334
- Park J., Ricotti M., Sugimura K., 2024, *MNRAS*, **528**, 6895
- Paxton B., et al., 2019, *ApJS*, **243**, 10
- Planck Collaboration 2020, *A&A*, **641**, A6
- Planck Collaboration et al., 2014, *A&A*, **571**, A16
- Prole L. R., Clark P. C., Klessen R. S., Glover S. C. O., 2022a, *MNRAS*, **510**, 4019
- Prole L. R., Clark P. C., Klessen R. S., Glover S. C. O., Pakmor R., 2022b, *MNRAS*, **516**, 2223
- Prole L. R., Schauer A. T. P., Clark P. C., Glover S. C. O., Priestley F. D., Klessen R. S., 2023, *MNRAS*, **520**, 2081
- Qin Y., Mesinger A., Park J., Greig B., Muñoz J. B., 2020, *MNRAS*, **495**, 123
- Qin Y., Hu R. C., Meynet G., Wang Y. Z., Zhu J. P., Song H. F., Shu X. W., Wu S. C., 2023, *A&A*, **671**, A62
- Qiu Y., et al., 2019, *ApJ*, **877**, 57
- Reig P., 2011, *Ap&SS*, **332**, 1
- Reis I., Fialkov A., Barkana R., 2020, *MNRAS*, **499**, 5993
- Reis I., Fialkov A., Barkana R., 2021, *MNRAS*, **506**, 5479
- Reis I., Barkana R., Fialkov A., 2022, *MNRAS*, **511**, 5265
- Rhodes J. D., Huff E., Masters D., Nierenberg A., 2020, *AJ*, **160**, 261
- Riaz R., Schleicher D. R. G., Bovino S., Vanaverbeke S., Klessen R. S., 2022a, arXiv e-prints, p. arXiv:2211.04413
- Riaz S., Hartwig T., Latif M. A., 2022b, *ApJ*, **937**, L6
- Riccio G., et al., 2023, *A&A*, **678**, A164
- Riley J., Mandel I., Marchant P., Butler E., Nathaniel K., Neijssel C., Shortt S., Vigna-Gómez A., 2021, *MNRAS*, **505**, 663
- Rivinius T., Carciofi A. C., Martayan C., 2013, *A&ARv*, **21**, 69
- Robertson B. E., et al., 2013, *ApJ*, **768**, 71
- Robertson B., et al., 2024, *ApJ*, **970**, 31
- Ryu T., Tanaka T. L., Perna R., 2016, *MNRAS*, **456**, 223
- Saad C. R., Bromm V., El Eid M., 2022, *MNRAS*, **516**, 3130
- Sadanari K. E., Omukai K., Sugimura K., Matsumoto T., Tomida K., 2023, *MNRAS*, **519**, 3076
- Sadanari K. E., Omukai K., Sugimura K., Matsumoto T., Tomida K., 2024, arXiv e-prints, p. arXiv:2405.15045
- Salvador-Solé E., Manrique A., Guzman R., Rodríguez Espinosa J. M., Gallego J., Herrero A., Mas-Hesse J. M., Marín Franch A., 2017, *ApJ*, **834**, 49
- Salvador-Solé E., Manrique A., Mas-Hesse J. M., Cabello C., Gallego J., Rodríguez-Espinosa J. M., Guzman R., 2022, arXiv e-prints, p. arXiv:2208.10426
- Sarmento R., Scannapieco E., Pan L., 2017, *ApJ*, **834**, 23
- Sarmento R., Scannapieco E., Cohen S., 2018, *ApJ*, **854**, 75
- Sarmento R., Scannapieco E., Côté B., 2019, *ApJ*, **871**, 206
- Sartorio N. S., et al., 2023, *MNRAS*,
- Schaerer D., 2002, *A&A*, **382**, 28
- Schaerer D., Marques-Chaves R., Xiao M., Korber D., 2024, arXiv e-prints, p. arXiv:2406.08408

- Schauer A. T. P., Liu B., Bromm V., 2019, *ApJ*, **877**, L5
- Schauer A. T. P., Drory N., Bromm V., 2020, *ApJ*, **904**, 145
- Schauer A. T. P., Glover S. C. O., Klessen R. S., Clark P., 2021, *MNRAS*, **507**, 1775
- Schauer A. T. P., Bromm V., Drory N., Boylan-Kolchin M., 2022, *ApJ*, **934**, L6
- Seager S., Sasselov D. D., Scott D., 1999, *ApJ*, **523**, L1
- Seager S., Sasselov D. D., Scott D., 2011, RECFAST: Calculate the Recombination History of the Universe, Astrophysics Source Code Library, record ascl:1106.026
- Senchyna P., Plat A., Stark D. P., Rudie G. C., 2023, *arXiv e-prints*, p. [arXiv:2303.04179](https://arxiv.org/abs/2303.04179)
- Sharda P., Krumholz M. R., 2022, *MNRAS*, **509**, 1959
- Sharda P., Menon S. H., 2024, *arXiv e-prints*, p. [arXiv:2405.18265](https://arxiv.org/abs/2405.18265)
- Sharda P., Federrath C., Krumholz M. R., 2020, *MNRAS*, **497**, 336
- Sharda P., Federrath C., Krumholz M. R., Schleicher D. R. G., 2021, *MNRAS*, **503**, 1214
- Shen X., Vogelsberger M., Boylan-Kolchin M., Tacchella S., Kannan R., 2023, *MNRAS*, **525**, 3254
- Sibony Y., Liu B., Simmonds C., Meynet G., Bromm V., 2022, *A&A*, **666**, A199
- Sims P. H., Pober J. C., 2020, *MNRAS*, **492**, 22
- Singh S., Subrahmanyan R., 2019, *ApJ*, **880**, 26
- Singh S., et al., 2022, *Nature Astronomy*, **6**, 607
- Skinner D., Wise J. H., 2020, *MNRAS*, **492**, 4386
- Smith B. D., Wise J. H., O’Shea B. W., Norman M. L., Khochfar S., 2015, *MNRAS*, **452**, 2822
- Sobacchi E., Mesinger A., 2013, *MNRAS*, **432**, 3340
- Sodini A., et al., 2024, *A&A*, **687**, A314
- Stacy A., Bromm V., Loeb A., 2011, *MNRAS*, **413**, 543
- Stacy A., Greif T. H., Klessen R. S., Bromm V., Loeb A., 2013, *MNRAS*, **431**, 1470
- Stacy A., Bromm V., Lee A. T., 2016, *MNRAS*, **462**, 1307
- Stacy A., McKee C. F., Lee A. T., Klein R. I., Li P. S., 2022, *MNRAS*, **511**, 5042
- Sugimura K., Matsumoto T., Hosokawa T., Hirano S., Omukai K., 2020, *ApJ*, **892**, L14
- Sugimura K., Matsumoto T., Hosokawa T., Hirano S., Omukai K., 2023, *arXiv e-prints*, p. [arXiv:2307.15108](https://arxiv.org/abs/2307.15108)
- Susa H., 2019, *ApJ*, **877**, 99
- Susa H., Hasegawa K., Tominaga N., 2014, *ApJ*, **792**, 32
- Szécsi D., Langer N., Yoon S.-C., Sanyal D., de Mink S., Evans C. J., Dermine T., 2015, *A&A*, **581**, A15
- Szécsi D., Agrawal P., Wünsch R., Langer N., 2022, *A&A*, **658**, A125
- Tacchella S., Bose S., Conroy C., Eisenstein D. J., Johnson B. D., 2018, *ApJ*, **868**, 92
- Tanikawa A., Yoshida T., Kinugawa T., Takahashi K., Umeda H., 2020, *MNRAS*, **495**, 4170
- Topping M. W., et al., 2024, *MNRAS*, **529**, 3301
- Tornatore L., Ferrara A., Schneider R., 2007, *MNRAS*, **382**, 945
- Toyouchi D., Inayoshi K., Li W., Haiman Z., Kuiper R., 2023, *MNRAS*, **518**, 1601
- Trussler J. A. A., et al., 2023, *MNRAS*, **525**, 5328
- Tseliakhovich D., Hirata C., 2010, *Phys. Rev. D*, **82**, 083520
- Tsiatsiou S., et al., 2024, *A&A*, **687**, A307
- Umeda H., Nagele C., 2024, *ApJ*, **961**, 146
- Vanni I., Salvadori S., Skúladóttir Á., Rossi M., Koutsouridou I., 2023, *MNRAS*, **526**, 2620
- Vanzella E., et al., 2023, *A&A*, **678**, A173
- Venditti A., Graziani L., Schneider R., Pentericci L., Di Cesare C., Maio U., Omukai K., 2023, *MNRAS*, **522**, 3809
- Venditti A., Bromm V., Finkelstein S. L., Calabrò A., Napolitano L., Graziani L., Schneider R., 2024, *arXiv e-prints*, p. [arXiv:2405.10940](https://arxiv.org/abs/2405.10940)
- Ventura E. M., Trinca A., Schneider R., Graziani L., Valiante R., Wyithe J. S. B., 2023, *MNRAS*, **520**, 3609
- Ventura E. M., Qin Y., Balu S., Wyithe J. S. B., 2024, *MNRAS*, **529**, 628
- Vigna-Gómez A., et al., 2025, *arXiv e-prints*, p. [arXiv:2503.17006](https://arxiv.org/abs/2503.17006)
- Vikaes A., Zackrisson E., Schaerer D., Visbal E., Fransson E., Malhotra S., Rhoads J., Sahlén M., 2022, *MNRAS*, **512**, 3030
- Visbal E., Barkana R., Fialkov A., Tseliakhovich D., Hirata C. M., 2012, *Nature*, **487**, 70
- Visbal E., Haiman Z., Bryan G. L., 2015, *MNRAS*, **453**, 4456
- Visbal E., Bryan G. L., Haiman Z., 2020, *ApJ*, **897**, 95
- Volpato G., Marigo P., Costa G., Bressan A., Trabucchi M., Girardi L., 2023, *ApJ*, **944**, 40
- Wang X., et al., 2024, *ApJ*, **967**, L42
- Welch B., et al., 2022, *Nature*, **603**, 815
- Windhorst R. A., et al., 2018, *ApJS*, **234**, 41
- Wollenberg K. M. J., Glover S. C. O., Clark P. C., Klessen R. S., 2020, *MNRAS*, **494**, 1871
- Wouthuysen S. A., 1952, *AJ*, **57**, 31
- Wyithe J. S. B., Loeb A., 2004, *Nature*, **432**, 194
- Xu H., Norman M. L., O’Shea B. W., Wise J. H., 2016, *ApJ*, **823**, 140
- Yoon S. C., Langer N., 2005, *A&A*, **443**, 643
- Yoon S. C., Langer N., Norman C., 2006, *A&A*, **460**, 199
- Yoon S. C., Dierks A., Langer N., 2012, *A&A*, **542**, A113
- Yoon J., et al., 2016, *ApJ*, **833**, 20
- Yoon J., et al., 2018, *ApJ*, **861**, 146
- Zackrisson E., Rydberg C.-E., Schaerer D., Östlin G., Tuli M., 2011, *ApJ*, **740**, 13
- Zackrisson E., et al., 2012, *MNRAS*, **427**, 2212
- Zackrisson E., et al., 2024, *MNRAS*, **533**, 2727
- Zahn O., Mesinger A., McQuinn M., Trac H., Cen R., Hernquist L. E., 2011, *MNRAS*, **414**, 727
- Zepeda J., et al., 2023, *ApJ*, **947**, 23
- Zhao M.-L., Wang S., Zhang X., 2024, *arXiv e-prints*, p. [arXiv:2412.19257](https://arxiv.org/abs/2412.19257)
- Zhu B., Gao L., 2024, *arXiv e-prints*, p. [arXiv:2410.16176](https://arxiv.org/abs/2410.16176)
- Zhu Y., et al., 2023, *ApJ*, **955**, 115
- Zuo Z.-Y., Song H.-T., Xue H.-C., 2021, *A&A*, **649**, L2
- de Lera Acedo E., et al., 2022, *Nature Astronomy*, **6**, 984
- de Mink S. E., Mandel I., 2016, *MNRAS*, **460**, 3545
- de Souza R. S., Ishida E. E. O., Johnson J. L., Whalen D. J., Mesinger A., 2013, *MNRAS*, **436**, 1555
- de Souza R. S., Ishida E. E. O., Whalen D. J., Johnson J. L., Ferrara A., 2014, *MNRAS*, **442**, 1640
- du Buisson L., et al., 2020, *MNRAS*, **499**, 5941

APPENDIX A: EXTRAPOLATION SCHEME FOR THE SPECTRA OF MASSIVE CHE STARS

We take the spectrum (i.e., specific luminosity) $L_\nu(t_{\text{ref}})$ at the last time step t_{ref} with converged TLUSTY results as the reference and calculate the spectrum $L_\nu(t)$ at a later time t with

$$L_\nu(t) = L_\nu(t_{\text{ref}})A(t) [B_\nu(T_{\text{eff}}(t))/B_\nu(T_{\text{eff}}(t_{\text{ref}}))]^\beta, \quad (\text{A1})$$

where $B_\nu(T_{\text{eff}})$ is the black-body spectrum for the temperature T_{eff} . $A(t)$ is a normalization factor set by the bolometric luminosity $L(t)$ with $\int_0^\infty L_\nu(t) d\nu = L(t)$, and the power-law index β is a free parameter that describes how strongly the spectral shape evolves. Since the bolometric luminosity $L(t)$ and effective temperature $T_{\text{eff}}(t)$ as functions of time throughout MS are already known from the analytical CHE model, our only task is to determine β . Interestingly, we find that the deviation of *spectral shape* from black-body is almost constant for atmospheres of CH stars with converged TLUSTY results, as shown in Fig. A1 for the $M_\star = 120 M_\odot$ case as an example. To be specific, we find $I_\nu(t)/B_\nu(T_{\text{eff}}(t)) \approx C(t)f_\nu$, where $I_\nu = L_\nu/(4\pi^2 R_\star^2)$ is the stellar surface intensity given the stellar radius R_\star . $C(t)$ is a normalization factor, and f_ν does not evolve with time. This implies that $L_\nu(t)/L_\nu(t_{\text{ref}}) \approx A(t)B_\nu(T_{\text{eff}}(t))/B_\nu(T_{\text{eff}}(t_{\text{ref}}))$, i.e., $\beta = 1$, which we take as the fiducial case.

To evaluate the uncertainty introduced by this extrapolation, we

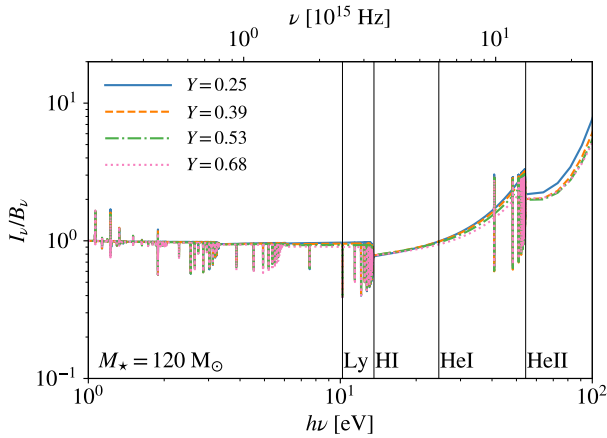


Figure A1. Deviation of spectral shape from black-body as a function of Y for the $M_\star = 120 M_\odot$ CHE model, in terms of the ratio of the intensity predicted by `TLUSTY` I_ν and the black-body intensity B_ν , normalized to have $I_\nu/B_\nu = 1$ at $h\nu = 1$ eV. The vertical lines label the characteristic energies for Lyman-band (Ly, $h\nu \sim 10.2 - 13.6$ eV), hydrogen (HI, $h\nu > 13.6$ eV), helium first (HeI, $h\nu > 24.6$ eV) and second (HeII, $h\nu > 54.4$ eV) ionizing photons. The weak evolution of the shape of I_ν/B_ν , with Y (and time) across a broad photon energy range (1 – 100 eV) allows us to derive the late-stage spectra of massive CH stars (that the stellar atmosphere code `TLUSTY` cannot handle) by simple extrapolation (see Eq. A1 and the text below).

further consider two alternative cases with $\beta = 0$ (no evolution) and $\beta = 2$ (enhanced evolution). We find by numerical experiments that our final results are insensitive to the choice of β for $\beta \in [0, 2]$ (Sec. 4). This partially due to the fact that T_{eff} only varies moderately ($\lesssim 10\%$) across the extrapolation for each star. Below, we only show the results for the fiducial case $\beta = 1$. Varying β in the range of $[0, 2]$ only changes $\epsilon_b(M_\star)$ for any band considered in Sec. 2 by no more than $\sim 10\%$ and does not affect our conclusions.

APPENDIX B: COMPARISON WITH THE RESULTS FROM BLACK-BODY SPECTRA

In general, compared with the spectrum computed by `TLUSTY`, the black-body spectrum, i.e., $L_\nu = 4\pi^2 R_\star^2 B_\nu(T_{\text{eff}})$, is slightly softer for a CH star but harder for an NR star. As a result, the enhancement in hydrogen ionizing photons by CHE is slightly weaker, while the enhancement in helium ionizing photons is significantly weaker, as shown in Fig. B1. Besides, the emission efficiency of Lyman-band photons $\epsilon_b^{\text{Ly}}(M_\star)$ is increased by CHE for $M_\star \lesssim 200 M_\odot$ by up to a factor of ~ 5 under black-body approximation, while the effect of CHE is more complex and weaker in the `TLUSTY` results. This highlights the importance of detailed stellar atmosphere modelling for Lyman-band photons.

APPENDIX C: IMPACT OF THE POP III IMF SLOPE AND POP II RECOVERY TIME ON REIONIZATION

Fig. C1 shows the effects of the Pop III IMF slope α on IGM ionization history, where three values $\alpha = 0$ (top-heavy), 1 (fiducial: log-flat), and 2.35 (bottom-heavy) are considered, under the fiducial SFE $f_{\star, \text{III}} = 0.003$ and recovery time $t_{\text{rec}} = 30$ Myr. α makes very small differences ($\Delta t_0 \lesssim 0.005$) but in different directions for the CH and NR models. With larger α IGM ionization is delayed in the NR

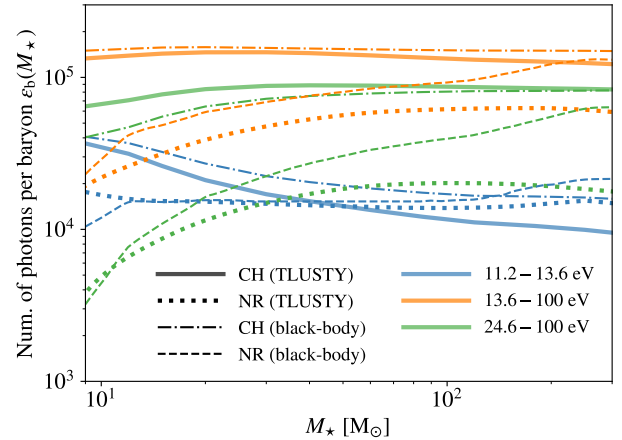


Figure B1. Similar to Fig. 3 but further showing the results from black-body spectra as the thin dash-dotted and dashed curves for CH and NR stars. For conciseness, only 3 bands are considered here: LW (11.2 – 13.6 eV, blue), ionizing radiation for hydrogen (13.6 – 100 eV, orange) and helium (24.6 – 100 eV, green). The black-body results for NR Pop III stars are taken from Sibony et al. (2022, see their fig. 2) based on the NR tracks evolved by the `GENEC` code with no mass loss from Murphy et al. (2021).

case, especially for $\alpha \gtrsim 1$, while it is slightly accelerated for the CH models. As shown in Fig. 3, the production efficiency $\epsilon_b^{\text{ion}}(M_\star)$ of ionizing photons increases (decreases slightly) for more massive NR (CH) Pop III stars, leading to different trends in the relation between the IMF-averaged efficiency $\epsilon_{\text{b,III}}^{\text{ion}}$ and α (Table 2). The effect of α on τ is weaker for CH stars compared with the NR case because given $f_{\star, \text{III}} = 0.003$, IGM ionization is rapid with CH stars, such that the relation between τ and $\epsilon_{\text{b,III}}^{\text{ion}}$ becomes sub-linear due to saturation and self-regulation of Pop III star formation by photoheating feedback.

Fig. C2 shows the results for different recovery times $t_{\text{rec}} = 10, 30,$ and 100 Myr given the fiducial Pop III SFE $f_{\star, \text{III}} = 0.003$ and IMF slope $\alpha = 1$. The impact of t_{rec} is even smaller with the same trend in the CH and NR cases: Ionization is delayed by larger t_{rec} . The reason is that increasing t_{rec} only suppresses Pop II star formation at $z \gtrsim 10$ (see Fig. 5) when ionization is still dominated by Pop III stars. In conclusion, α and t_{rec} only have minor effects ($\lesssim 10\%$) on the ionization history compared with those of SFE and stellar evolution (Sec. 4.2). However, they play more important roles in shaping the 21-cm signal (Sec. 4.3).

APPENDIX D: POWER SPECTRA OF THE 21-CM SIGNAL VS WAVE-NUMBER AT REDSHIFTS 8 AND 10

Figs. D1, D2, and D3 show the power spectra of the 21-cm signal for $k \sim 0.03 - 1 h \text{ cMpc}^{-1}$ at two redshifts: $z = 8$ (left panel) and 10 (right panel), where $f_{\star, \text{III}}$, α , and t_{rec} are varied, receptively, while keeping the other parameters fixed to their fiducial values. Here, the general spectral shape mainly reflects the transition from EoH to EoR. Before the transition, deep in EoH, the power spectrum is relatively flat with less than a factor of 10 variations across $k \sim 0.03 - 1 h \text{ cMpc}^{-1}$. During the transition, the large-scale power decrease significantly due to the negative contribution of cross correlations between neutral fraction and IGM temperature fluctuations. The spectrum becomes flatter approaching the end of transition, when the distribution of neutral/ionized regions becomes the dominant factor. Thereafter, the signal decays to zero when the IGM is fully ionized.

All models considered here are experiencing the transition from

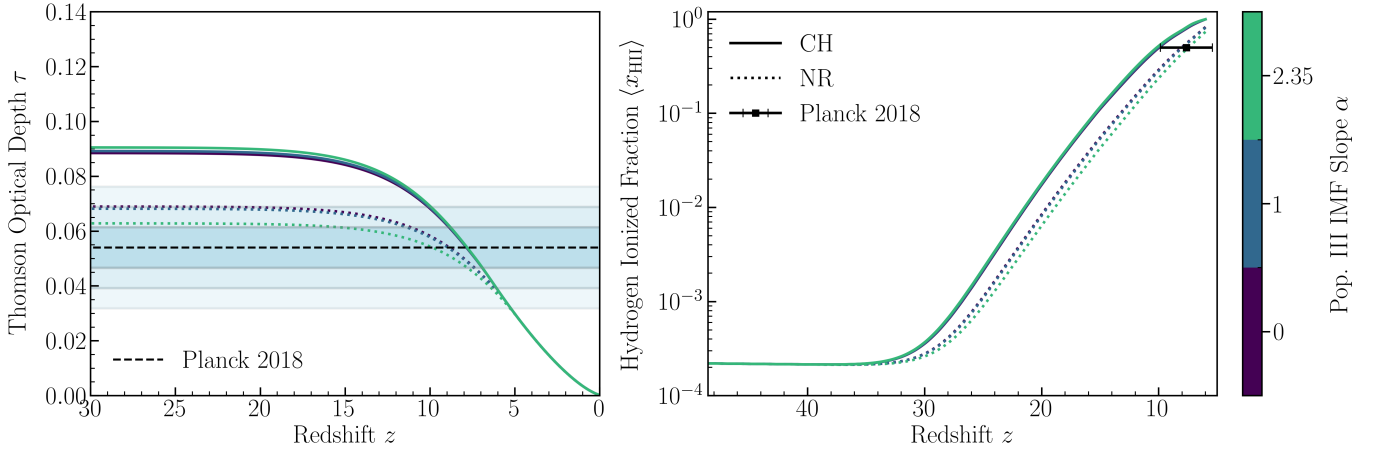


Figure C1. Ionization history. Same as Fig. 6 but varying the Pop III IMF slope α (0, 1, and 2.35) with fixed SFE $f_{\star, \text{III}} = 0.003$ and recovery time $t_{\text{rec}} = 30$ Myr.

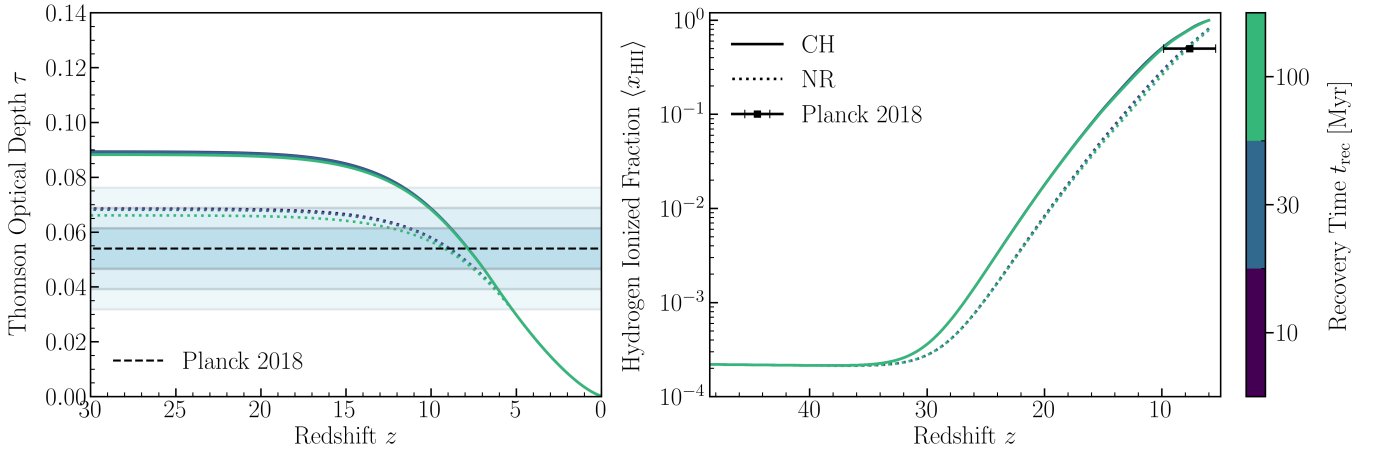


Figure C2. Ionization history. Same as Fig. 6 but varying the recovery time t_{rec} (10, 30, and 100 Myr) with fixed Pop III SFE $f_{\star, \text{III}} = 0.003$ and IMF slope $\alpha = 1$.

EoH to EoR at $z = 8$, which is typically in a more advanced stage for higher $f_{\star, \text{III}}$ and for CH stars compared with NR stars given $f_{\star, \text{III}} \gtrsim 0.003$. The effects of α and t_{rec} are always small. The transition has not happened at $z = 10$ for the models that are consistent with the observational constraints from reionization (i.e., $f_{\star, \text{III}} \lesssim 0.002$ for CH star and $f_{\star, \text{III}} \lesssim 0.004$ for NR stars), where the volume-averaged ionized fraction of the IGM remains below 30% (Fig. 6). However, the other, more extreme models show the transition feature at $z = 10$, where the power is suppressed by CHE in the full range $k \sim 0.03 - 1 \text{ h cMpc}^{-1}$ considered here with stronger effects at larger scales (smaller k). At $z = 10$, the large-scale power increases with t_{rec} , which delays X-ray heating and enhances IGM temperature fluctuations. The effects of α are still negligible, while $f_{\star, \text{III}}$ only has a significant impact when the transition happens (for $f_{\star, \text{III}} \gtrsim 0.003$).

For all models considered here, the predicted $\Delta^2(k)$ at $z \sim 8-10$ is not only below the upper limit placed by HERA Collaboration (2023) at $k \approx 0.24 \text{ cMpc}^{-1}$ by at least 2 orders of magnitude (triangles in Figs. D1-D3) but also lower than the upper limit $\Delta^2 \lesssim 4700 \text{ mK}^2$ from LOFAR at a larger scale $k \sim 0.05 \text{ cMpc}^{-1}$ (Mertens et al. 2025) by at least a factor of ~ 1000 .

This paper has been typeset from a $\text{\TeX}/\text{\LaTeX}$ file prepared by the author.

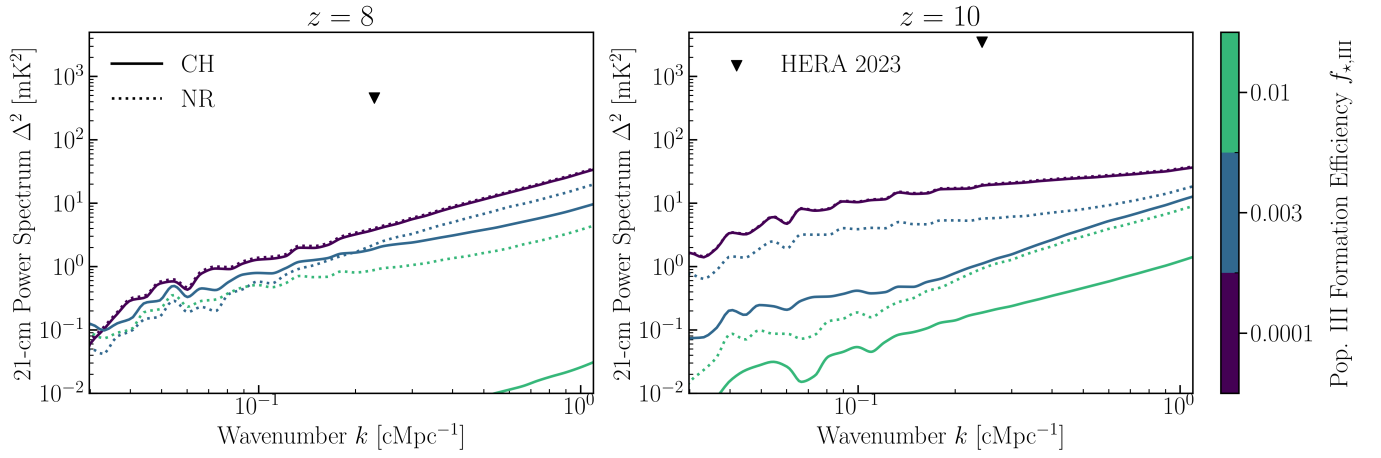


Figure D1. 21-cm power spectrum for $z = 8$ (left) and $z = 10$ (right) with varying $f_{\star, \text{III}} \sim 10^{-4} - 0.01$ and fixed $\alpha = 1$ and $t_{\text{rec}} = 30$ Myr. As in Fig. 8, the dotted (solid) curves show the results for the NR (CH) Pop III stellar evolution models, and the results for higher $f_{\star, \text{III}}$ are denoted by lighter colours. 2σ upper limits observed by HERA Collaboration (2023) are shown by the triangles.

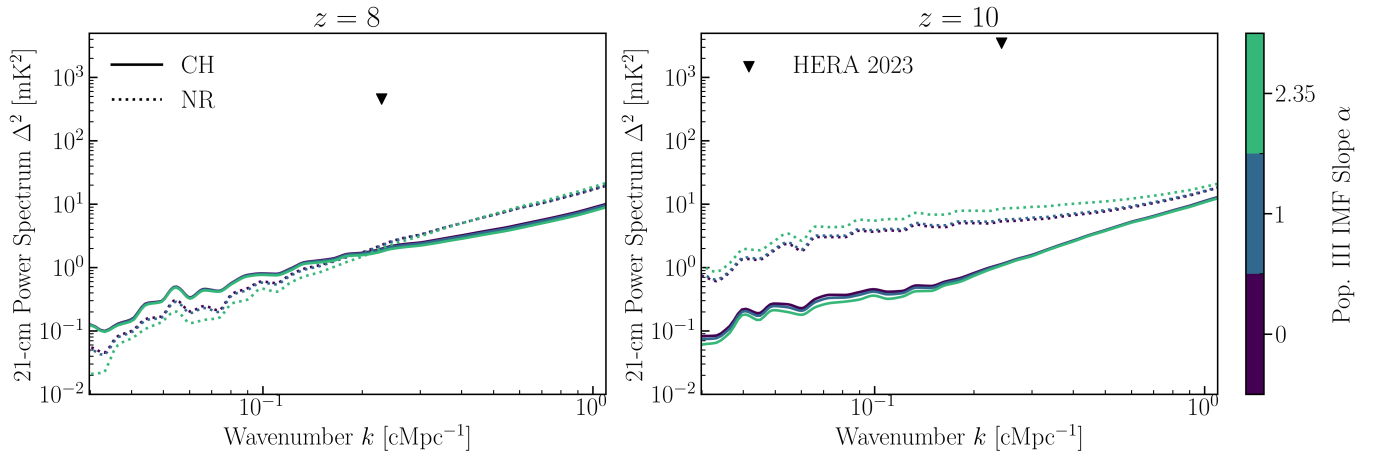


Figure D2. 21-cm power spectrum. Same as Fig. D1 but varying the Pop III IMF slope α (0, 1, and 2.35) with fixed SFE $f_{\star, \text{III}} = 0.003$ and recovery time $t_{\text{rec}} = 30$ Myr.

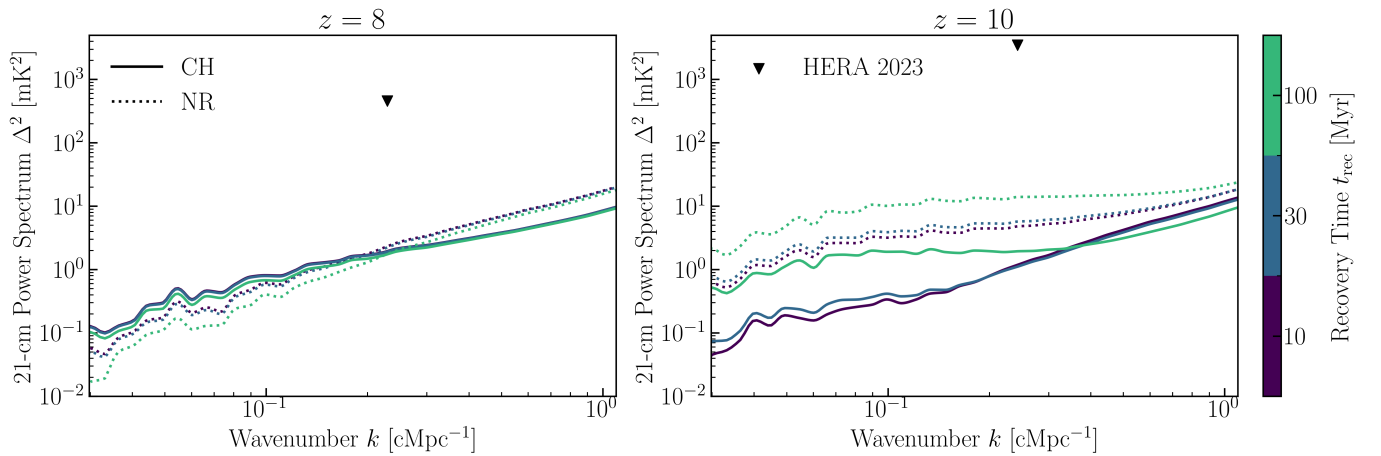


Figure D3. 21-cm power spectrum. Same as Fig. D1 but varying the recovery time t_{rec} (10, 30, and 100 Myr) with fixed Pop III SFE $f_{\star, \text{III}} = 0.003$ and IMF slope $\alpha = 1$.